

Advanced targeted curcumin delivery using biodegradable hierarchical microspheres with calcium pectinate matrix and hyaluronic acid moieties for enhancing colitis amelioration



Jin Feng ^{a,*}, Zhen Wang ^{a,b}, Xingyu Zhao ^{a,b}, Lujing Xu ^a, Cong Teng ^a, Songbai Liu ^c, Wuyang Huang ^{a,*}, Ying Li ^{a,*}

^a Institute of Agro-product Processing, Jiangsu Academy of Agricultural Sciences, 50 Zhongling Street, Nanjing, 210014, China

^b School of Food and Biological Engineering, Jiangsu University, 301 Xuefu Road, Zhenjiang 212013, China

^c Department of Food Science and Nutrition, Innovation Center of Yangtze River Delta, Zhejiang University, 866 Yuhangtang Road, Hangzhou 310058, China

ARTICLE INFO

Keywords:

Hierarchical microspheres
Lipid nanocarriers
Inflammation-targeted delivery
Curcumin
Ulcerative colitis
Differentiation-44 receptor

ABSTRACT

Oral targeted delivery systems for food bioactive compounds have attracted considerable attention for improving the efficiency of nutritional interventions. In this study, a hierarchical curcumin carrier with sequence-targeting capability was fabricated to mitigate colitis through a convenient and environmentally friendly approach. Initially, curcumin-loaded nanostructured lipid carriers (NLC) with hyaluronic acid (HA) moieties (HA-NLC) were prepared using ovalbumin-HA conjugates as emulsifiers. Subsequently, HA-NLC was immobilized within a calcium pectinate matrix using electrospray, leading to the formation of supramolecular microspheres (HA-NLC@MPs) approximately 140 µm in size. Results suggested that the pectin matrix preserved the integrity of the carrier and prevented curcumin leakage during transit through the upper gastrointestinal tract, while selectively degrading in response to colon bacteria. Moreover, the exposed HA moieties on the released HA-NLC facilitated the transcellular absorption of curcumin by inflamed colonic enterocytes through cluster of differentiation-44 receptor-mediated endocytosis. *In vitro* and *in vivo* studies demonstrated predominant curcumin accumulation in the colorectal tissues of colitis mice using HA-NLC@MPs as carrier. Curcumin delivered via HA-NLC@MPs demonstrated superior effects in alleviating colitis compared with that in the nanocarriers, through the modulation of macrophage polarization, TLR4/MyD88/NF-κB signaling cascade, and gut microbiota homeostasis.

1. Introduction

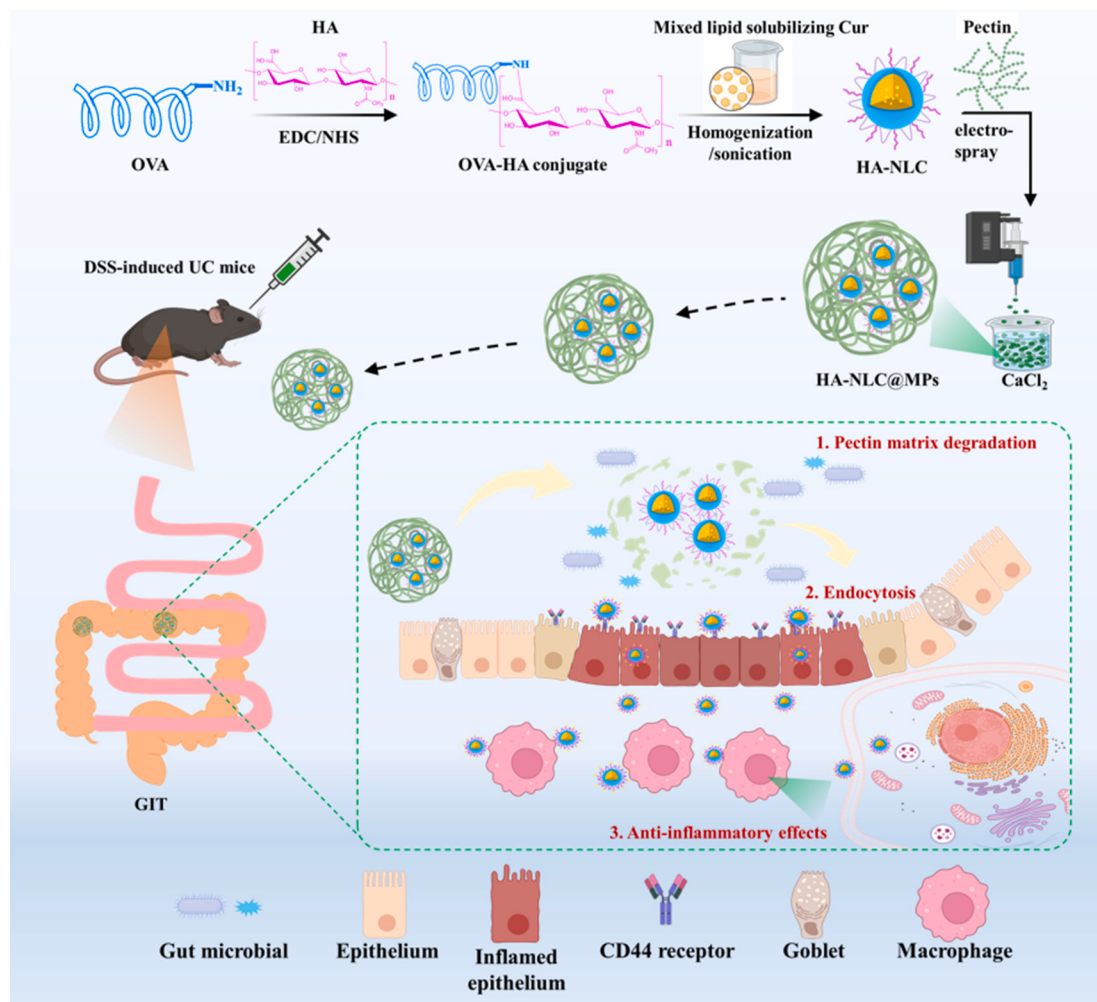
Bioactive nutraceuticals derived from nature sources, such as peptides, polyphenols, and polyunsaturated lipids, have been identified and isolated. Numerous researches consistently underscore their crucial role in the intricate relationship between diet and health (Wu, Liu, Li, & Feng, 2024). To tackle challenges hindering their use in nutritional interventions, such as low chemical stability and intestinal absorption, various nanocarriers, like nanoparticles (McClements, 2020), nano-emulsions (Esfanjani, Assadpour, & Jafari, 2018), and nanocomposites (Akbari-Alavijeh, Shaddel, & Jafari, 2020), have been developed in the past decade. In these systems, the functionalities of the nutraceuticals and related mechanisms are dependent on their biological fate after entering systemic circulation from the upper gastrointestinal tract (GIT) (Sabet, Rashidinejad, Melton, & McGillivray, 2021). Nevertheless,

pioneering studies have shown that the bio-efficacy of nutraceuticals after oral administration is also highly associated with the interactions among the nutraceuticals (both the parent molecules and metabolites), gut microbiota, and immune/endocrine systems, which are regarded as indirect health effects (Tian et al., 2022). Therefore, it is crucial for nutraceuticals to be delivered and accumulated at the target sites with appropriate biological fates to enhance their bio-efficacy effectively.

The smart delivery systems, equipped with pre-designed release mechanisms, adsorption routines, and metabolic pathways for loaded cargoes, are crucial for optimizing the health benefits of nutraceuticals by modulating their digestive fate (Hossen et al., 2019). The lower GIT part, such as colon, served as the host for most gut microbes and have a strong relationship with human health (de Vos, Tilg, Van Hul, & Cani, 2022). Chronic inflammatory bowel diseases like ulcerative colitis (UC) activate inflammatory pathways, disrupt the intestinal barrier, cause

* Corresponding authors.

E-mail addresses: fengjinju@163.com (J. Feng), wuyanghuang@hotmail.com (W. Huang), hijoly@163.com (Y. Li).



Scheme 1. Schematic illustration of the fabrication of biodegradable hierarchical microspheres (HA-NLC@MPs) loaded with Cur and their inflammation-targeted delivery effects in UC mice.

intestinal dysbiosis, and increase harmful gut microbiota (Chen et al., 2023; Liang et al., 2023). Compared with clinical drugs, nutritional intervention represents a more sustainable, safe, and comprehensive approach (Tie et al., 2022). To maintain the colon homeostasis through nutritional intervention, it's essential to reduce nutraceutical loss in the upper digestive tract and improve their absorption in the inflamed colon area (Naeem et al., 2020). In this context, targeted delivery systems for the lower GIT should employ hierarchical structures that are resistant to digestion but responsive to gut microbiota in the colon, thereby facilitating precise release of the loaded cargo at specific sites (Tian et al., 2022).

Hierarchical delivery systems with nanocarriers immobilized in polysaccharide matrix have been employed for targeted delivery to the distal gut (Yuan et al., 2022). Polysaccharides like pectin and inulin resist digestion in the upper GIT but are susceptible to the carbohydrate-active enzymes (CAZymes) produced by gut microbiota. Consequently, these polysaccharides could effectively inhibit the digestion of vehicles and the release of loaded agent within the upper GIT. Subsequently, these polysaccharides were degraded in colon, and the nanocarriers loaded with bioactive compounds were accumulated at the colon site to reshape the gut microbiota and mitigate inflammatory lesions (Tian et al., 2022; Xing et al., 2024).

The cluster of differentiation-44 (CD44) receptor is a transmembrane glycoprotein expressed on the surfaces of enterocytes and macrophages (Lu et al., 2023), known for its sensitivity to inflammatory responses. The overexpression of CD44 in colonic enterocytes during colitis has

been extensively documented (Vafaei et al., 2016; Xu et al., 2022; Zhu et al., 2024). Furthermore, CD44 plays a key role in receptor-mediated endocytosis (Tie et al., 2022). Hyaluronic acid (HA), a natural hydrocolloid available as food additives and dietary supplements, acts as a specific ligand for CD44 receptors (Tan, Yao, Jafari, Sun, & Wang, 2023). HA has been utilized to modify the surfaces of nano-vehicles, thereby enhancing the absorption of loaded cargo in inflamed enterocytes and macrophages through CD44-mediated endocytosis (Chen et al., 2023; Feng et al., 2025; Tie et al., 2022).

Lipid-based carriers possess a multitude of advantages, including enhanced biocompatibility and biodegradability, controlled drug release, extended circulation times, and ease of large-scale manufacturing. Nanostructured lipid carriers (NLC) contain both liquid and solid lipids in the lipid phase resulting in an imperfect crystalline structure (Spinazzi et al., 2024). The solid lipids serve as physical barriers that impede the migration of hydrophobic substances, whereas the liquid lipid create more loading space to accommodate the core agent (Salminen, Helgason, Kristinsson, Kristbergsson, & Weiss, 2017). NLC have been utilized to enhance the cellular absorption and antioxidant/anti-inflammatory capacity of Cur in our previous reports (Feng et al., 2020; Feng et al., 2025; Li et al., 2022). Herein, we propose an innovative hypothesis that designing distal gut-targeted delivery systems based on HA-decorated NLC and with a hierarchical structure could enhance the bio-efficacy of loaded Cur for treating colitis. To validate the hypothesis, NLC with HA moieties (HA-NLC) were prepared using an ovalbumin (OVA)-HA conjugate as emulsifiers to encapsulate

curcumin (Cur), is a naturally occurring polyphenol with superb anti-inflammatory capacity (Tsuda, 2018). Subsequently, they were entrapped within pectin matrix, resulting in supramolecular microspheres with hierarchical structure (HA-NLC@MPs). The pectin matrix preserved the integrity of the carrier and prevented the leakage of the loaded cargo in the upper GIT, and it only began to degrade in the colon in the presence of CAZymes produced by the gut microbiota. Simultaneously, the exposed HA moieties bind with CD44 in the inflamed colon area of the dextran sulfate sodium (DSS)-induced colitis mice, thereby promoting the absorption of Cur by colonic enterocytes through receptor-mediated endocytosis and enhancing its bio-efficacy for alleviating inflammatory lesions (Scheme 1).

2. Experimental section

2.1. Materials

Cur (>95 %), OVA (from egg white, ≥90 %), and medium-chain triglycerides (MCT, 55.50 % caprylic triglyceride/44.50 % capric triglyceride) were purchased from Yuanye Bio-Technology Co., Ltd. (Shanghai, China). The sodium salt of HA (M_w 9.8 kDa, ≥98 %, Fig. S1) was purchased from FuRuiDa Pharmaceutical Company, Ltd. (Shandong, China). 1-(3-Dimethylaminopropyl)-3-ethylcarbodiimide hydrochloride (EDC, 98 %), N-hydroxysuccinimide (NHS, 98 %), and indocyanine green 780 (IR780, ≥95 %) were purchased from Aladdin Biochemical Technology Co., Ltd. (Shanghai, China). Glyceryl tristearate (GTS, ~90 %), pectin (from citrus peel, galacturonic acid content 82 %, Fig. S2), porcine pepsin (3200–4500 U mg⁻¹), porcine pancreatin (8 × USP specifications), porcine bile salt (cholic acid sodium salt, ~50 %; deoxycholic acid sodium salt, ~50 %), Cell Counting Kit 8 (CCK8), recombinant human Interleukin-1 beta protein (IL-1 β , >95 %), lipopolysaccharide (LPS, ≥97 %), verapamil hydrochloride (Ver, ≥99 %), and phorbol 12-myristate 13 acetate (PMA, ≥99 %) were purchased from Sigma-Aldrich Corp. (St. Louis, USA). Fetal bovine serum (FBS), Dulbecco's modified Eagle medium (DMEM), RPMI 1640 medium, N-2-hydroxyethylpiperazine-N-2-ethane sulfonic acid (HEPES) buffer (1 M), penicillin-streptomycin (100×), Hank's balanced salt solution (HBSS), and CellROXTM Deep Red were purchased from Thermo Fisher Scientific (Massachusetts, USA). DSS (36,000–50,000 Da, colitis grade, ≥98 %) was purchased from MP Biomedicals Co., Ltd. (Southern California, USA). Caco-2, HT29-MTX (E12), and THP-1 cells were purchased from the Cell Resource Center (Peking Union Medical College Headquarters of National Infrastructure of Cell Line Resource, Beijing, China).

2.2. Preparation of NLC and HA-NLC loaded with cur

OVA-HA conjugates were synthesized as detailed in a recent report from our laboratory (Feng et al., 2025). Hyaluronic acid (HA) at a concentration of 1.0 % (w/v) was combined with EDC and NHS to achieve a 1:1:1 M ratio of EDC: NHS: glucuronic acid residues. The mixture was incubated at ambient temperature for 1 h to activate the carboxyl groups. Subsequently, an equal volume of OVA solution at 4.0 % (w/v) was gradually added to the HA solution, and the reaction continued for 24 h under ambient conditions. After the reaction, the mixture was adjusted to pH 7.0, and the solution was centrifuged at 8000 rpm for 10 min. The supernatant containing the OVA-HA conjugates was then transferred to a dialysis bag with a molecular weight cutoff of 8000–14,000 Da and dialyzed against ultrapure water for 48 h. Finally, the solution in bag was lyophilized to yield OVA-HA conjugates. The yield percentage, defined as the weight ratio of lyophilized OVA-HA conjugates to the combined weight of initial OVA and HA, was calculated to be 82.56 %. The weight-average molecular weight (M_w) of OVA and OVA-HA conjugate was calculated using the gel permeation chromatography (GPC), which were 44.75 kDa (Fig. S3A) and 54.49 kDa (Fig. S3B), respectively. These findings confirmed the successful conjugation of one OVA molecule to one HA molecule via an amidation

reaction catalyzed by EDC/NHS. Additionally, by integrating the peak areas from the GPC profiles, the purity of the OVA-HA conjugates was determined to be 90.21 % (Fig. S3B).

NLC was prepared using OVA as emulsifiers, while HA-NLC was prepared using OVA-HA conjugates as emulsifiers (Li et al., 2022). In brief, after melting at 80 °C, GTS was mixed with preheated MCT at a mass ratio of 4:1. Cur (0.5 %, relative to the weight of the GTS/MCT mixture) was solubilized in the hot lipid phase mentioned above. The hot lipid phase was mixed with the OVA or OVA-HA conjugate solution (corresponding to an OVA concentration of 2.0 wt%) preheated at 80 °C for 30 min at a volume ratio of 1:9, which was then homogenized at 12,000 rpm for 5 min. Thereafter, ultrasonication at 600 W (2 s on/2 s off) for 10 min was performed to reduce the particle size. The temperature was maintained at 80 °C throughout the above procedure to prevent lipid crystallization. After ultrasonication, the sample was immediately transferred to an ice-water bath for 1 h for carrier crystallization.

2.3. Preparation of HA-NLC@MPs loaded with Cur

The HA-NLC@MPs were prepared using an electrospray method as described previously (Wang et al., 2022) with a JDF05 electrospraying machine (Changsha nanoapparatus instrument technology Co., Ltd). Briefly, the HA-NLC suspension was combined with an equal volume of aqueous pectic polysaccharide (2.0 %, w/v), and the mixture was homogenized at 8000 rpm for 10 min. The electrospray parameters were as follows: syringe volume of 10 mL, flow rate of 15 mL/h, voltage of 11 kV, receiving solution of 0.3 % CaCl₂ (w/v), and a 3.0 cm distance from the receiving solution. The microspheres were collected by centrifugation and washed with ultrapure water to remove the free Ca²⁺. This washing process was repeated several times, and the samples were stored at 4 °C before use.

2.4. Characterization of the delivery systems

The hydrodynamic diameter (D_z), polydispersity index (PDI), and ζ -potential of both the NLC and HA-NLC were measured using a Malvern Nano-ZS 90 zeta-sizer (Malvern, United Kingdom) at ambient temperature. To mitigate multiple scattering phenomenon, the samples were diluted with ultrapure water before testing.

The droplet size of HA-NLC@MPs was measured using a Mastersizer 3000 laser diffraction particle size analyzer (Malvern Instruments, UK). The $D_{4,3}$ value, representing the volume mean diameter, was obtained to reflect the dimension of the microspheres (Jiang & Charcosset, 2022).

For transmission electron microscopy (TEM) observation, a copper grid support film (200 mesh) was used to hold aliquots of diluted samples. After drying, a single drop of aqueous phosphotungstic acid (2.0 wt %) was applied to stain the samples for 1 min. The excess dye was removed by filter paper and the samples were dried at ambient temperature overnight. Morphological observations were conducted at a voltage of 200 kV with a JEM-1230 (HR) microscope (JEOL, Japan).

For optical microscope observation, place an appropriate volume of microsphere dispersion on a microscope slide. Their morphology was examined using a 4 × objective lens at first, and the magnification was adjusted as necessary to capture images.

2.5. In vitro digestion assay

An aliquot (10 mL) of the Cur carrier was mixed with an equal volume of simulated gastric fluid (SGF, pH 2.0, containing 6 mM CaCl₂, 120 mM NaCl, 5 mM KCl, and 3.2 mg/mL pepsin). The mixture was adjusted to pH 2.0 and incubated at 37 °C with stirring at 100 rpm for 1 h. Subsequently, the pH of the digesta was adjusted to 7.0 and mixed with an equal volume of simulated small intestinal fluid (SIF, pH 7.0, containing 6 mM CaCl₂, 120 mM NaCl, 5.0 mg/mL bile salts, and 8.0 mg/mL pancreatin). The system was further incubated at 37 °C with

stirring at 100 rpm for 2 h.

Simulated colon fluid (SCF) was prepared by mixing fresh rat feces (5.0 wt%) with PBS (pH 7.0). The mixture was centrifuged, and the resulting supernatant was filtered through a 220 nm membrane (Wang et al., 2022). The digesta from the small intestine phase was mixed with an equal volume of SCF, which was immediately transferred to an anaerobic box with a gas-generating pack to create an anaerobic environment. The whole system was incubated at 100 rpm for a duration of 21 h. At predetermined time points, samples were collected and replaced with an identical volume of simulated fluid.

The microstructure of both NLC and HA-NLC was observed using TEM as mentioned above. Meanwhile, the degradation process of HA-NLC@MPs was monitored by confocal laser scanning microscopy (CLSM). Components such as proteins, lipids, and polysaccharides within HA-NLC@MPs were stained with Nile blue (0.1 % w/v, Excitation: 633 nm), Nile red (0.1 % w/v, Excitation: 488 nm), and Calcofluor White (Excitation: 400 nm), respectively. The samples were transferred onto slides and examined using an Ultra View VoX CLSM microscope (PerkinElmer, USA).

To analysis the Cur release in the GIT, samples were centrifuged at 10000 rpm for 10 min. The supernatant was then extracted with ethyl acetate thrice. Subsequently, the organic phases were combined, evaporated, and dissolved in acetonitrile for quantification of the Cur content using HPLC. The cumulative release rate was determined as follows (Ban et al., 2020):

$$\text{Cumulative release rate (\%)} = \frac{\text{amount of Cur in the release medium}}{\text{total amount of Cur}} \times 100\% \quad (1)$$

To monitor the lipolysis process of the delivery systems in SIF, the pH of the digesta was maintained at pH 7.0 ± 0.05 by automatic titration with 0.05 M NaOH using an 842 Titrand unit (Metrohm AG, Herisau, Switzerland). The extent of lipolysis was assessed by measuring the fraction of released free fatty acids (FFAs), using the following equation (Wang et al., 2024):

$$\text{FFAs (\%)} = \frac{V_{\text{NaOH}} \times C_{\text{NaOH}} \times M_{\text{lipid}}}{W_{\text{lipid}} \times 2} \times 100\% \quad (2)$$

Herein, V_{NaOH} is the volume (L) of the NaOH solution consumed to neutralize the FFAs, C_{NaOH} is the molarity (0.05 mol L^{-1}) of the NaOH solution, M_{lipid} is the average molecular weight of lipids (g/mol), and W_{lipid} is the total weight of lipids in chyme (g).

2.6. Cell culture and cytotoxicity assay

The Caco-2 cells were cultured at 37 °C in a 5 % CO₂ atmosphere using DMEM medium supplemented with 10 % FBS, 1 % penicillin-streptomycin, and 1 % HEPES buffer. Cells between 20 and 40 passages were employed to ensure consistent cellular phenotypes throughout the study.

An aliquot (100 µL) of a mixed Caco-2/HT29-MTX (E12) cell suspension (7:3) at a density of $4 \times 10^5/\text{mL}$ was seeded into each well of a 96-well plate and incubated for 48 h afterwards to allow cell attachment. Subsequently, free Cur, Cur in NLC, and Cur in HA-NLC were dispersed in the medium at final concentrations of 30, 50, 80, and 100 µM, and the cells were cultured for an additional 20 h. Cells treated with only DEME medium served as the control. Each group contained 6 replicates. Ten microliters of CCK8 and 90 µL of fresh medium were used to replace the suspension, and the cells were further incubated for 4 h. The absorbance at 450 nm of each well was recorded with a microplate

reader and the cell viability was calculated using the formula (Tie et al., 2022):

$$\text{Cell viability (\%)} = \frac{A_{\text{sample}} - A_{\text{blank}}}{A_{\text{control}} - A_{\text{blank}}} \times 100\% \quad (3)$$

where A_{sample} , A_{blank} , and A_{control} represents the absorbance values of the treated, control, and blank wells at 450 nm, respectively.

2.7. Monolayer permeation assay

In accordance with a previous study (Li et al., 2023), a mixture of Caco-2 cells and HT29-MTX (E12) cells (7:3) totaling 1.5 mL were seeded on the apical side (AP) of the Transwell insert plates (6-well, 3.0 µm pore size, 24 mm diameter, Corning CoStar Corp., Cambridge, MA, USA). The cells were cultured for 21 days to form integrated monolayers. Transepithelial electrical resistance (TEER) values of the monolayers were measured using a Millicell® Electrical Resistance System (Millipore Corporation, Billerica, MA, USA), and only monolayers with TEER values exceeding $300 \Omega/\text{cm}^2$ were selected for transport studies. The medium from both AP and basolateral (BL) side was replaced with pre-warmed fresh PBS. The cells were rinsed with PBS and equilibrated at 37 °C for 20 min. Subsequently, the monolayers were treated with IL-1β solution (2 µg/L) for 24 h to induced inflammatory responses, and monolayers incubated with blank medium serving as controls. The expression of the CD44 receptors were analyzed by immunofluorescence

staining tests with mouse anti-human CD44 monoclonal antibodies (ab16728, abcam) and Alexa Fluor® 555-labelled goat anti-mouse IgG (H + L) (ab150118, abcam).

To investigate the transportation of Cur from AP to BL side, 1.5 mL of the free Cur, Cur in NLC, and Cur in HA-NLC of 50 µM were added to the AP side, while 2.6 mL of the fresh PBS was added to the BL side. To investigate the transportation of Cur from the BL to AP side, 2.6 mL of Cur (50 µM, free or encapsulated) was added to the BL side, along with 1.5 mL of fresh PBS to the AP side. The systems were then incubated at 37 °C for 4 h. At predetermined time intervals, 100 µL of the medium was withdrawn from the BL (AP) side, which was extracted three times with 2 volumes of ethyl acetate. The extracts were evaporated to dryness, and the residues were dissolved in acetonitrile for Cur quantification. The apparent permeability coefficient (P_{app} , cm/s) across the Caco-2 monolayers was calculated using the following equation:

$$P_{\text{app}} \text{ (cm/s)} = \frac{dQ}{dt \times A \times C} \quad (4)$$

where dQ/dt is the translocation of the loaded Cur from the donor to receptor compartments (µmol/s), A is the membrane area (cm²), and C is the initial concentration of the prepared samples in the donor compartment (µg/mL).

On the other hand, the efflux ratio was calculated using the following equation:

$$\text{Efflux ratio} = \frac{P_{\text{app}} \text{ (BL} \rightarrow \text{AP)}}{P_{\text{app}} \text{ (AP} \rightarrow \text{BL)}} \quad (5)$$

where $P_{\text{app}} \text{ (BL} \rightarrow \text{AP)}$ and $P_{\text{app}} \text{ (AP} \rightarrow \text{BL)}$ are the permeability values from the BL to AP side and from the AP to BL side, respectively.

To investigate the effects of CD44-mediated endocytosis and P-glycoprotein (P-gp)-mediated efflux on the transcellular absorption of Cur formulations, the Caco-2 monolayers were pre-incubated with HA

(0.05 mg/mL) or Ver (100 μM) at 37 °C for 1.0 h, and various Cur formulations (50 μM) were subsequently added to the AP or BL sides for 4 h in the presence of inhibitors for the bidirectional transport assay, and the P_{app} and efflux ratio values were calculated as described above.

2.8. In vitro anti-inflammatory assay

The present study used a Caco-2/HT29-MTX (E12)/THP-1 dual-chamber cell model to investigate the anti-inflammatory capacities (Hu et al., 2020). Caco-2/HT29-MTX (E12) monolayers were prepared as previously outlined. THP-1 cells were cultured in RPMI 1640 medium supplemented with 10 % FBS and differentiated into macrophage-like cells in the presence of 50 ng/mL phorbol ester for 48 h. Subsequently, these cells were seeded in 6-well plates (3×10^5 cells per well) and cultured for an additional 24 h. The Caco-2 monolayers supported by transwell inserts were placed into multiple plate wells pre-seeded with THP-1 cells. Various Cur formulations of 50 μM were added to the AP side and incubated for 8 h to allow transcellular absorption. Subsequently, LPS at a final concentration of 0.5 μg/mL was added to the BL side to induce inflammatory responses in the cells. Negative controls were treated with only DEME blank medium, while positive controls received only LPS. The dual-chamber cell model was then incubated for an additional 12 h.

Immunofluorescence staining was conducted to analyze the expression of occludin and claudin-1. The monolayers were treated with rabbit anti-human anti-occludin (abs154942, absin) or anti-claudin 1 (abs122916, absin) antibody, followed by Alexa Fluor® 555- or Alexa Fluor® 488-labelled goat anti-rabbit IgG (H + L) (ab150078 and ab150077, abcam). The fluorescence signals were then recorded by CLSM and semi-quantified by ImageJ software (version 1.8.0, National Institutes of Health, Bethesda, MD, USA). TEER values of the monolayers were recorded using the Millicell®-electrical resistance system as mentioned above. For the detection of reactive oxygen species (ROS), cells in the BL side were treated with CellROX™ Deep Red (5.0 μM) for 30 min (Feng et al., 2025), and the red fluorescence signals were then recorded by CLSM. Levels of cellular tumor necrosis factor alpha (TNF-α) and interleukin-6 (IL-6) in the supernatant were assessed using enzyme-linked immunosorbent assay (ELISA) kits (mlbio, Shanghai, China).

2.9. In vivo biodistribution assay

All the animal experiments were conducted in accordance with the animal use regulations and guidelines of the Jiangsu Academy of Agricultural Sciences, with the protocol approved by the Institutional Animal Care and Use Committee (approved protocol number: IACUC-202301215). The study was carried out in compliance with the Animal Research: Reporting *In Vivo* Experiments (ARRIVE) guidelines 2.0, and the U.K. Animals (Scientific Procedures) Act, 1986 and associated guidelines. Male C57BL/6 mice (6–7 weeks old, weighing 20–22 g) were procured from SPF (Beijing) Biotechnology Co., Ltd. They were housed under a 12 h light/dark cycle at 25 °C and allowed a 7-day acclimatization period. To induce an acute experimental colitis model, mice were administered 3 % DSS in their drinking water for 7 days.

To evaluate the biodistribution of the carriers in the GIT, IR780 was used as a fluorescent probe and encapsulated into the carriers. Male C57BL/6 mice with DSS-induced colitis received oral administration of free IR780 or IR780 encapsulated in NLC, HA-NLC, or HA-NLC@MPs, each at an equivalent to 0.5 mg IR780/kg body weight. Fluorescence imaging was performed using a multifunctional *in vivo* imaging system (IVIS Spectrum, PerkinElmer, USA) at 3 h, 12 h, and 24 h post-administration. After 24 h, the mice were euthanized, and the digestive tract were harvested and the fluorescence images were captured (Xu et al., 2022). CD44 expression in the colon tissue of the control and DSS groups was analyzed by immunofluorescence staining tests with rabbit anti-mouse CD44 antibody (ab189524, abcam) and Alexa Fluor® 555-labelled goat anti-rabbit IgG (H + L) (ab150078, abcam).

2.10. In vivo intervention of Cur-loaded carriers on DSS-induced colitis

According to a previous report (Liang et al., 2023), thirty-six mice were randomly assigned into different groups, including control group, DSS group, free Cur group, Cur in NLC group, Cur in HA-NLC group, and Cur in HA-NLC@MPs group ($n = 6$ per group). Mice in the intervention groups received oral doses equivalent to 50 mg/kg/day of Cur for 7 days. Subsequently, 3.0 % DSS (w/w) was administered instead of drinking water for 7 days to induce colitis.

During that time, body weight and disease activity index (DAI) of the mice were recorded, following the criteria from a previous work (Cao et al., 2021). On day 8, mice were euthanized and the colon length was measured. Sections of colon tissue were fixed in 4 % paraformaldehyde for histological and immunofluorescence analysis. The expression of occludin, claudin 1, CD86 and CD206 were analyzed by immunofluorescence staining tests with rabbit anti-mouse anti-occludin (abs154942, absin), anti-claudin 1 (abs122916, absin), anti-CD86 (ab242142, abcam), and anti-mannose receptor (ab64693, abcam) antibodies, followed by Alexa Fluor® 555- or Alexa Fluor® 488-labelled goat anti-rabbit IgG (H + L) (ab150078 and ab150077, abcam). The fluorescence signals were then recorded by CLSM and semi-quantified by ImageJ software.

The remaining tissue was assessed for malonaldehyde (MDA), total superoxide dismutase (T-SOD), catalase (CAT), myeloperoxidase (MPO) and nitric oxide (NO) using commercial kits. Additionally, inflammatory cytokines including TNF-α, interleukin-1β (IL-1β), IL-6 and interleukin-10 (IL-10) were detected in serum using corresponding ELISA kits (mlbio, Shanghai, China).

Western blotting analysis was carried out to assess the expression levels of inflammation-related proteins. Proteins in colon tissue was extracted using RIPA lysis buffer and quantified by the bicinchoninic Acid (BCA) method. An aliquot (30 μg) of the proteins were separated on a 12 % SDS-PAGE gel and transferred to a polyvinylidene fluoride (PVDF) membrane. The membrane was blocked with 3 % bovine serum albumin (BSA) for 1.5 h in tris-buffered saline (TBS) containing 0.05 % Tween-20 at room temperature. The samples were incubated with rabbit anti-mouse anti-toll-like receptor 4 (TLR4, ab218987, abcam), anti-myeloid differentiation primary response 88 (MyD88, S0B0647, starter), anti-Nuclear Factor-κB p65 subunit (NF-κB p65, S0B0549, starter), and anti-β-actin (abs171598, absin), followed by horseradish peroxidase (HPR) conjugated goat anti-rabbit IgG secondary antibody (ab288151, abcam). The bands were exposed with an enhanced chemiluminescence kit (Thermo Fisher Scientific, Cat#34580) and semi-quantified using ImageJ software (version 1.8.0) normalized by β-actin.

2.11. Intestinal microbiota analysis

The composition of gut microbiota in mouse feces was analyzed using 16S rDNA amplicon sequencing technology, and a small fragment library was constructed at Biomarker Technologies Co., Ltd. (Beijing, China). The sample processing included DNA extraction and quantification, PCR amplification, fluorescence-based quantification, library preparation, and sequencing on the NovaSeq platform. Data analysis focused on gut microbiota composition, relative abundance, complexity, diversity, and inter-group differences, and was performed using the company's network cloud platform.

2.12. Quantification of the short-chain fatty acids (SCFAs)

Briefly, 100 mg of colonic content was transferred to centrifuge tubes and combined with 20 μL of diluted sulfuric acid (50 %, v/v), 995 μL of diethyl ether, and 5 μL of diluted 2-ethylbutyric acid (v/v = 1/100) (Liang et al., 2023). The mixture was thoroughly vortexed and subjected to sonication in an ice bath for 30 min to facilitate complete SCFAs release, followed by centrifugation at 10000 g for 15 min. The supernatant was treated with anhydrous sodium sulfate to eliminate residue

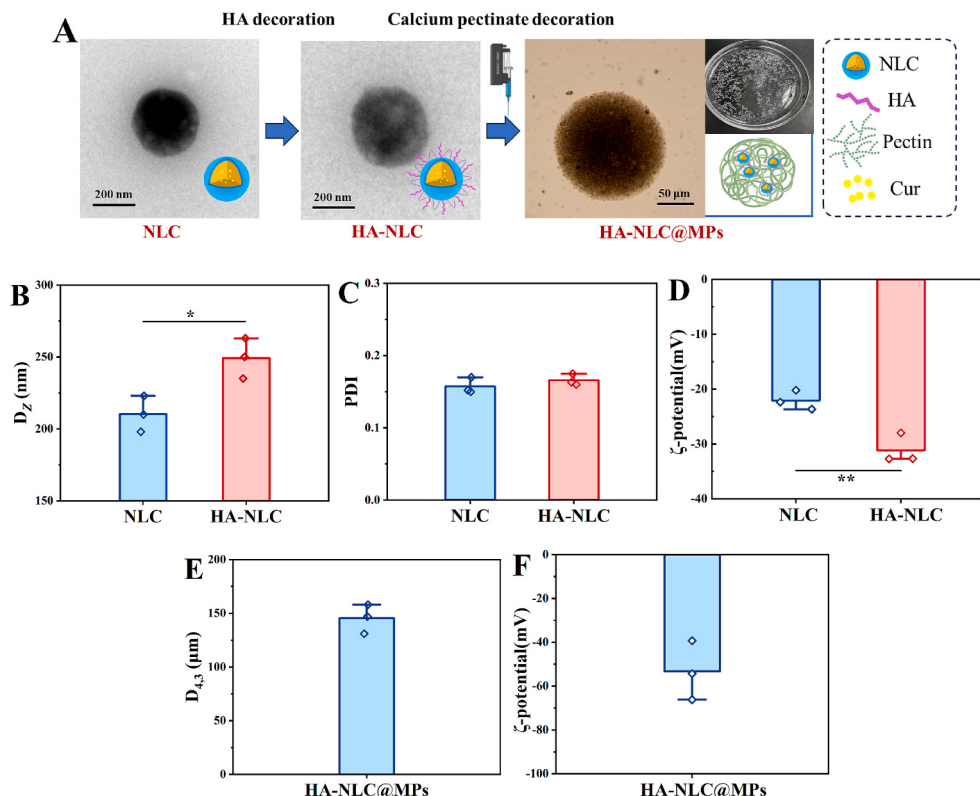


Fig. 1. Microstructure of the three Cur delivery systems. (A) TEM images. (B) D_z , (C) PDI, and (D) ζ -potential of the NLC and HA-NLC. (E) $D_{4,3}$ and (F) ζ -potential of the HA-NLC@MPs. * and ** represent $p < 0.05$ and $p < 0.01$, respectively.

water, centrifuged again, and filtered through a $0.22 \mu\text{m}$ membrane. The content of acetic acid, propionic acid, *n*-butyric acid, isobutyric acid, and *n*-valeric were quantified by an Agilent 7890B gas chromatography instrument equipped with an Agilent HP-INNOWAX capillary column ($30 \text{ m} \times 0.25 \text{ mm} \times 0.25 \mu\text{m}$).

2.13. Long-term toxicity assay

C57BL/6 J mice was randomly divided into four groups, including control group, Cur in NLC group, Cur in HA-NLC group, and Cur in HA-NLC@MPs group ($n = 6$ per group). The mice in different groups were administrated the vehicles with doses equivalent to 50 mg/kg/day of Cur for 8 weeks. All the samples were the same as that applied in the colitis model as described above. At the end of the test, the mice were euthanized and the hearts, livers, spleens, lungs, kidneys and testicles were fixed in 4 % paraformaldehyde solution, embedded in paraffin, and then stained with hematoxylin-eosin (H&E) for histological evaluation. Serum samples were collected and the biochemistry indexes, such as alanine transferase (ALT), aspartate transferase (AST), total bilirubin (TBIL), creatinine (Crea), urea, blood urea nitrogen (BUN), total cholesterol (T-CHO), and triglyceride (TG) were determined (Li et al., 2024).

2.14. Statistical analysis

Statistical analysis was conducted using GraphPad Prism 5.0 software (GraphPad Software Inc., San Diego, CA, USA). Each analysis employed either the student's *t*-test or one-way analysis of variance (ANOVA). Statistical significance was considered for p values <0.05 . Unless otherwise specified, results were presented as mean \pm standard deviation (SD).

3. Results and discussions

3.1. Characterization of the Cur carriers

The morphology of NLC, HA-NLC and HA-NLC@MPs was depicted in Fig. 1A. Both NLC and HA-NLC are nano-scale in size. The D_z of NLC was $210.33 \pm 12.50 \text{ nm}$ (Fig. 1B), consistent with our prior research (Li et al., 2022). On the other hand, the D_z of HA-NLC was significantly larger compared with NLC, measuring $249.34 \pm 14.01 \text{ nm}$. OVA-HA conjugates were synthesized in this study and employed as emulsifiers for HA-NLC. The formation of covalent bonds between these two biopolymers was confirmed by GPC analysis (Fig. S3). Therefore, the higher D_z of HA-NLC compare with that of NLC might be attributed to the presence of the HA moieties (Feng et al., 2025). The PDI values of both nanocarriers were well below 0.2 (Fig. 1C), indicating homogenous and unimodal size distributions. HA-NLC exhibited a more pronounced negative surface charge compared with NLC, primarily due to the conjugation of HA moieties (Fig. 1D). HA-NLC@MPs were fabricated through the electrospray of a blended solution comprising HA-NLC and pectic polysaccharides into Ca^{2+} solution, which effectively crosslinked the carboxyl groups on the galacturonic acid residues to yield gelled microspheres with abundant “egg-box” junction zones (Chen et al., 2021). Simultaneously, the HA-NLC nanocarriers were entrapped within the gel matrix. The $D_{4,3}$ of the HA-NLC@MPs was $145.30 \pm 13.58 \mu\text{m}$ (Fig. 1E), which was thousand times larger than the diameter of HA-NLC. Apart from the filling effects of HA-NLC, the large size of the HA-NLC@MPs could also arise from the swelling of the polysaccharide matrix under neutral conditions. The surface of HA-NLC@MPs also carried negative charges resulting from the deprotonation of the carboxyl groups (Fig. 1F). As a result, three stable Cur delivery systems were successfully prepared, and their digestive fate in the simulated GIT was explored in the next section.

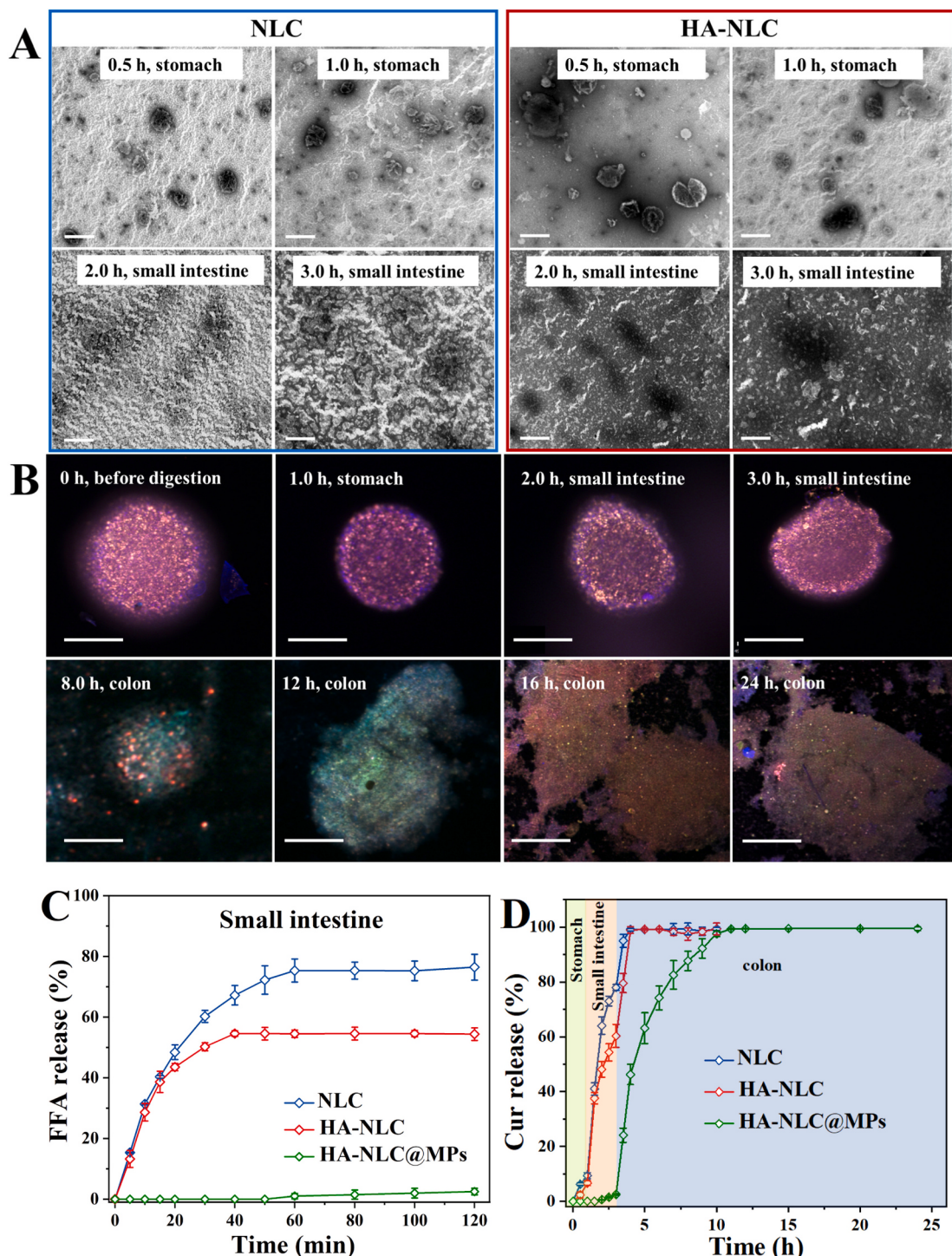


Fig. 2. *In vitro* digestive behaviors of NLC, HA-NLC, and HA-NLC@MPs. (A) Microstructure evolution of the NLC and HA-NLC during the stomach and small intestine phases by TEM. (B) Microstructure evolution of the HA-NLC@MPs during the stomach, small intestine, and colon phases by CLSM. (C) FFAs release profiles of the carriers during the small intestine phase. (D) Cumulative Cur release during the stomach, small intestine and colon phases. Bar in A: 200 nm. Bar in B: 100 μ m.

3.2. The pectin matrix facilitates a colon-targeted Cur accumulation

The colonic transport efficiency of the loaded cargo is closely linked to the stability of the carriers as they pass through the stomach and small intestinal phases. Disruption of the carriers in the upper GIT leads to the leakage of the loaded cargo (Yuan et al., 2022). As depicted in Fig. 2A, the microstructure of the NLC remained stable in the stomach phase. However, after 2 h of digestion, the boundary and shape of the NLC became less distinct, likely due to the replacement of emulsifiers by bile

salt and the lipolysis of the lipid core of the NLC in the small intestine phase. The morphology of the NLC became even more blurred after 3 h of digestion. Similar evolution patterns could be observed for HA-NLC, although with the difference that the microstructure remained more intact after 2 h of digestion. Furthermore, no intact nanoparticles could be discerned for either NLC or HA-NLC during the colon phase at 8.0 h (Fig. S4).

As shown in the CLSM images in Fig. 2B, the structure of HA-NLC@MPs remained stable during the stomach phase but transformed

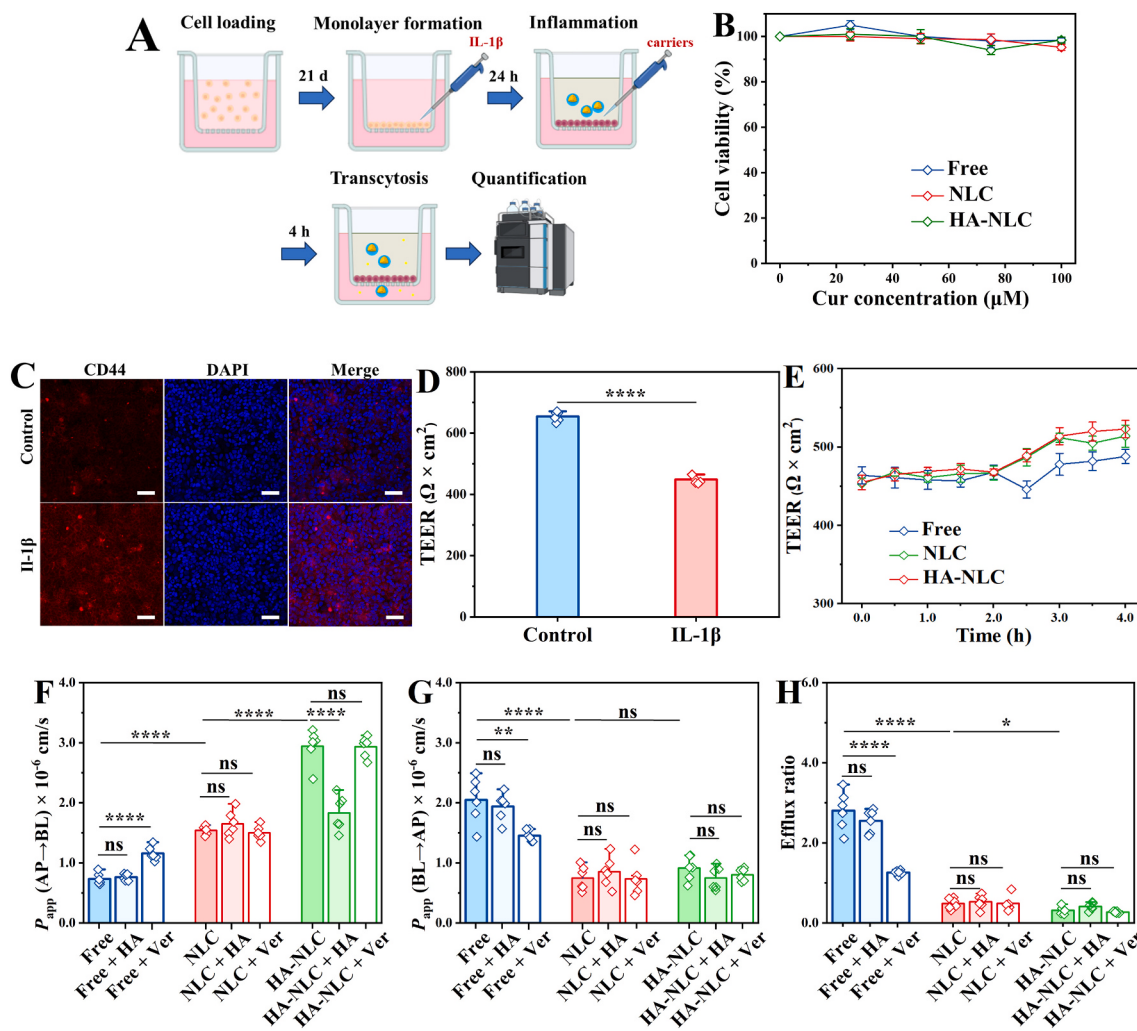


Fig. 3. Transcellular efficiency of Cur carriers across the inflamed Caco-2/HT29-MTX (E12) monolayers. (A) Schematic illustration of the Cur permeation tests. (B) Cytotoxicity of different forms of Cur. (C) CD44 expression and (D) TEER values in normal and inflamed monolayers. (E) Changes in the TEER values during the monolayer permeation test. (F) P_{app} (A \rightarrow B), (G) P_{app} (B \rightarrow A), and (H) efflux ratio values of different Cur formulations in the presence of HA or Ver. *, **, ***, and **** represent $p < 0.05$, $p < 0.01$, $p < 0.001$ and $p < 0.0001$, respectively. ns: not significant. Bar in C: 100 μm .

from spherical to irregular shape upon entering the small intestine. Notably, their structure integrity did not collapse in SIF, thereby preventing the release of the embedded HA-NLC. The HA-NLC@MPs were resistant to intestinal digestion because of the steric hindrance effects of the pectin matrix, which is not susceptible to pancreatic hydrolysis. However, during the colon phase, the structure of the HA-NLC@MPs disintegrated gradually and was destroyed completely within 16 h. This phenomenon likely resulted from the degradation of the pectin-based matrix under the influences of CAZymes in SCF such as β -glucosidase (Luo et al., 2021). The SCF was centrifuged at 24 h, and the supernatant was collected for the analysis of the morphology and particle size of the released HA-NLC. The released particles exhibited a spherical morphology with a diameter of 200 nm, and the D_z was 246.73 nm (Fig. S5), consistent with that of the fresh HA-NLC. Given that the colon phase contains fewer lipase and protease, the microstructure of the released HA-NLC remained intact during this phase. Consequently, the released HA-NLC will prolong the retention of encapsulated Cur in the gastrointestinal tract due to the specific binding between the HA moieties and the CD44 receptors.

The lipolysis of the carriers was monitored during the small intestine phase. Both NLC and HA-NLC showed a rapid FFAs release within the first 20 min in the SIF, after which the release reached a plateau (Fig. 2C). The highest release percentage were $76.44 \pm 4.23\%$ for NLC

and $54.38 \pm 2.10\%$ for HA-NLC. Previous studies have highlighted that HA contributes to the digestive stability of oil droplets by providing steric and repulsive electrostatic forces (Aguilera-Garrido, del Castillo-Santaella, Galisteo-González, José Gálvez-Ruiz, & Maldonado-Valderrama, 2021). By contrast, the lipolysis rate of the HA-NLC@MPs was limited, with a highest FFAs release percentage below 10 % by the end of the test. These findings corresponded with the microstructure changes of these carriers during the small intestine phase (Fig. 2A-B). Further investigation was conducted on Cur release in all three phases. As shown in Fig. 2D, the three carriers exhibited limited Cur release in the stomach phase. NLC and HA-NLC showed rapid Cur leakage during the small intestine phase, with highest release percentage of $78.0 \pm 1.12\%$ and $60.33 \pm 4.20\%$, respectively. This result suggested that the majority of Cur in NLC and HA-NLC was released during this stage. Due to their resistance to intestinal digestion, $<5.0\%$ of encapsulated Cur was released from the HA-NLC@MPs during the combined stomach and small intestine phases. However, the HA-NLC@MPs exhibited rapid Cur release in the SCF, achieving nearly 100 % release after 10 h. Overall, the HA-NLC@MPs promoted the predominant Cur accumulation in the colorectal region. Previous studies have also suggested the potential role of the pectic polysaccharide matrix in facilitating targeted Cur release in colon (Luo et al., 2021; Wang et al., 2022).

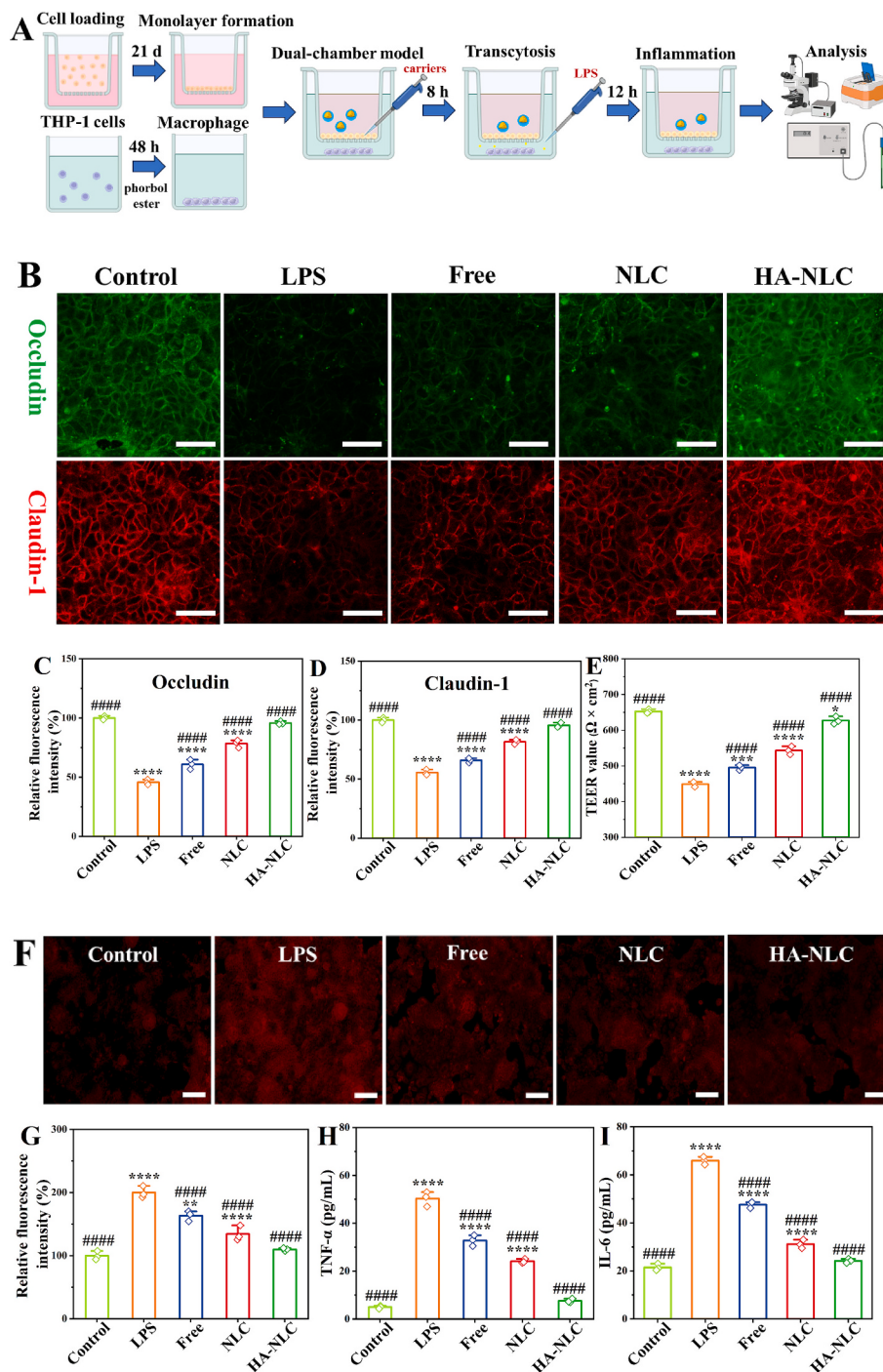


Fig. 4. *In vitro* anti-inflammatory effects analysis. (A) Schematic illustration of the anti-inflammatory tests using the dual-chamber cell models. (B) Immunofluorescence images of epithelial tight junction proteins. The fluorescence density of (C) occludin and (D) claudin-1. (E) The TEER values. (F) The fluorescence images and (G) fluorescence density of the macrophages treated with CellROX™ Deep Red. Pro-inflammatory cytokine levels of (H) TNF- α and (I) IL-6. *, **, ***, and **** represent $p < 0.05$, $p < 0.01$, $p < 0.001$ and $p < 0.0001$, respectively, compared with the control; #, ##, ###, and ##### represent $p < 0.05$, $p < 0.01$, $p < 0.001$, and $p < 0.0001$, respectively, compared with the LPS group. Bar in B and F: 100 μm .

3.3. HA moieties promote the transcellular absorption of loaded Cur and its anti-inflammatory capacity

In this section, the transcellular absorption of the HA-NLC released from the microspheres was investigated, with NLC serving as control. As depicted in Fig. 3A, the monolayers were simulated by IL-1 β to induce an inflammatory response. Free Cur, Cur in NLC, or Cur in HA-NLC were introduced to the AP side, and the permeation amount was quantified. Note that the cell viability was well above 95 % in Cur concentration

range of 20–100 μM , suggesting that these three formulations were not toxic to the cells (Fig. 3B). The CD44 receptor expression on the monolayers was assessed using the immunostaining method, as depicted in Fig. 3C. The control group exhibited very faint red fluorescence signals, suggesting a low level of CD44 expression. Following simulation with IL-1 β , the fluorescence intensity increased significantly, which indicated the overexpression of these receptors. Previous studies reported similar findings when the Caco-2 cells were treated with IL-1 β /LPS (Feng et al., 2025; Vafaei et al., 2016).

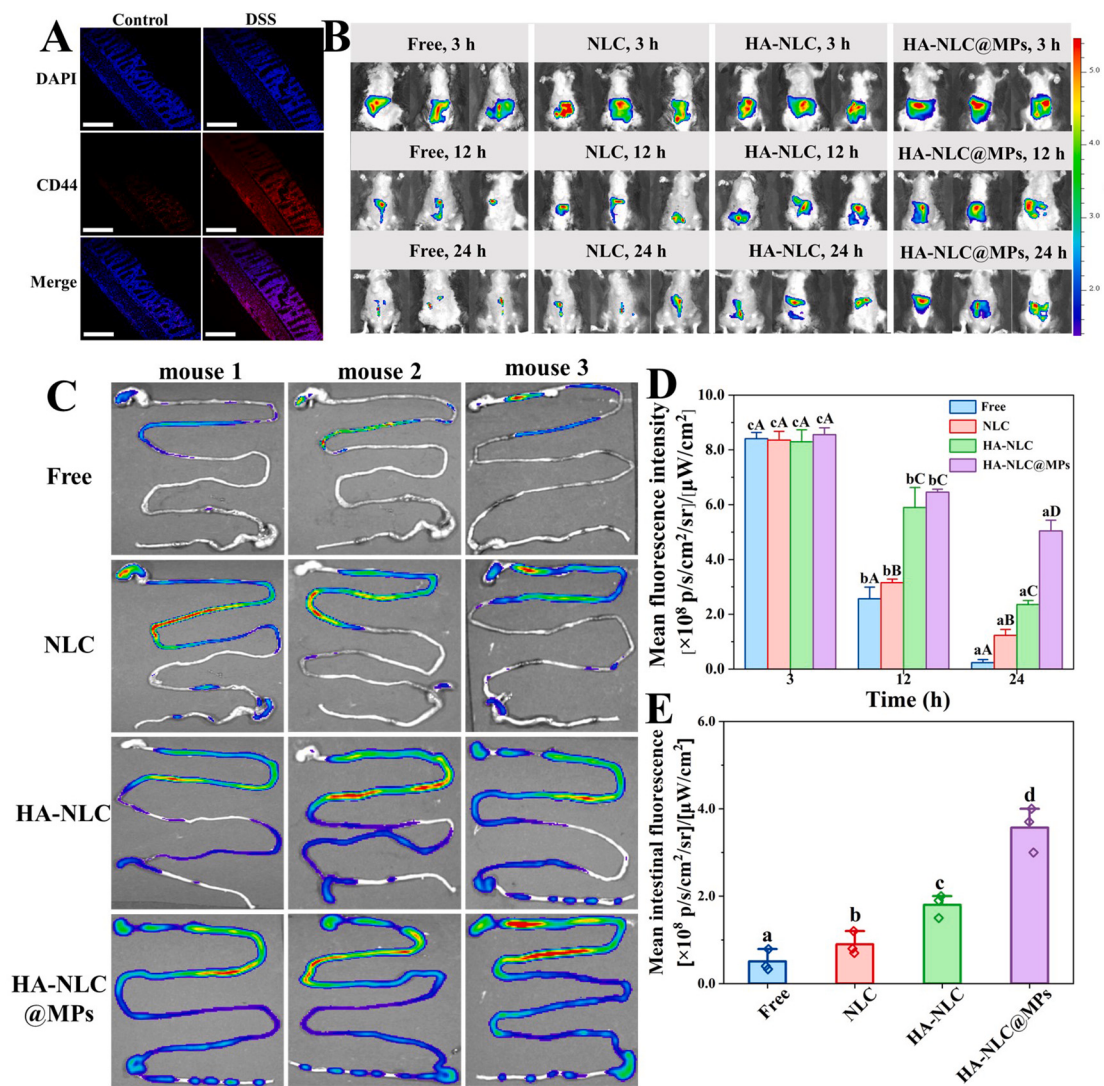


Fig. 5. *In vivo* biodistribution of IR780 probe in different carriers. (A) Immunofluorescent staining of anti-CD44 antibodies in colon tissue from the control and DSS groups. (B) Fluorescence images of the UC mice at 3, 12, and 24 h post oral administration of different formulations, and (D) the corresponding semiquantitative analysis results. (C) Fluorescence images of the GIT at 24 h post oral administration of different formulations, and (E) the corresponding semiquantitative analysis results. Significant differences ($p < 0.05$) were indicated by different lowercase letters in D between different time points following oral administration of the same carrier. Significant differences ($p < 0.05$) were indicated by different uppercase letters in D when comparing different types of carriers at the same time point. Significant differences ($p < 0.05$) were indicated by different lowercase letters in E. Bar in A: 200 μ m.

Note that the IL-1 β treatment reduced the TEER values from above $600 \Omega \text{ cm}^{-2}$ to approximately $450 \Omega \text{ cm}^{-2}$ ($p < 0.0001$) (Fig. 3D) because this cytokine impaired the expression of epithelial tight junction proteins (Chen et al., 2023). However, despite inflammation, the TEER values of the inflamed Caco-2/HT29-MTX (E12) monolayers remained above $300 \Omega \text{ cm}^{-2}$, which is a critical threshold for permeation analysis (Bao et al., 2020). During the first 2 h of the intestinal absorption test, the TEER value remained almost constant in the presence of free or loaded Cur. Subsequently, the TEER value showed a slight increase over time (Fig. 3E). These findings suggest that the permeation of different Cur formulations occurred primarily through the transcellular pathways rather than the paracellular pathways.

The P_{app} value in the AP \rightarrow BL direction was below $1 \times 10^{-6} \text{ cm/s}$ for free Cur (Fig. 3F), indicating poor intestinal absorption. Conversely, the P_{app} value of Cur in NLC was nearly twice that of the free Cur. Nano-encapsulation enhances Cur solubility in the medium and activates specific endocytosis pathways, thereby improving its cellular uptake (McClements, 2020). Cur in HA-NLC exhibited the highest P_{app} (AP \rightarrow BL) value of $2.94 \pm 0.29 \times 10^{-6} \text{ cm/s}$, likely due to the CD44 receptor-

mediated endocytosis pathways. Chen and coauthors reported that the cellular uptake efficiency by inflamed macrophages increase by 1.3-fold when the whey protein isolate-dextran nanoparticles were conjugated with HA moieties (Chen et al., 2023). Moreover, the HA pretreatment led to a significant decrease ($p < 0.0001$) in the P_{app} (AP \rightarrow BL) value of Cur in HA-NLC (Fig. 3F). By contrast, the P_{app} (AP \rightarrow BL) value of free Cur and Cur in NLC showed only slight change in the presence of HA ($p > 0.05$). This confirmed the involvement of CD44 receptor-mediated endocytosis in the transcellular absorption of Cur in HA-NLC (Tie et al., 2022).

The P_{app} (BL \rightarrow AP) value of free Cur was over 2-fold that of the Cur in either NLC or HA-NLC (Fig. 3G), and free Cur showed a high efflux ratio of approximately 3.0 (Fig. 3H). In the presence of Ver, a P-gp inhibitor, the P_{app} (BL \rightarrow AP) value of free Cur decreased significantly ($p < 0.01$), along with a substantial reduction in the efflux ratio to approximately one-third of its original value ($p < 0.0001$). These results suggested that Cur was a potential substrate for the P-gp protein (Li et al., 2023). Conversely, the efflux ratio of Cur in NLC or HA-NLC remained below 0.5 and exhibited insignificant change ($p > 0.05$) in the presence

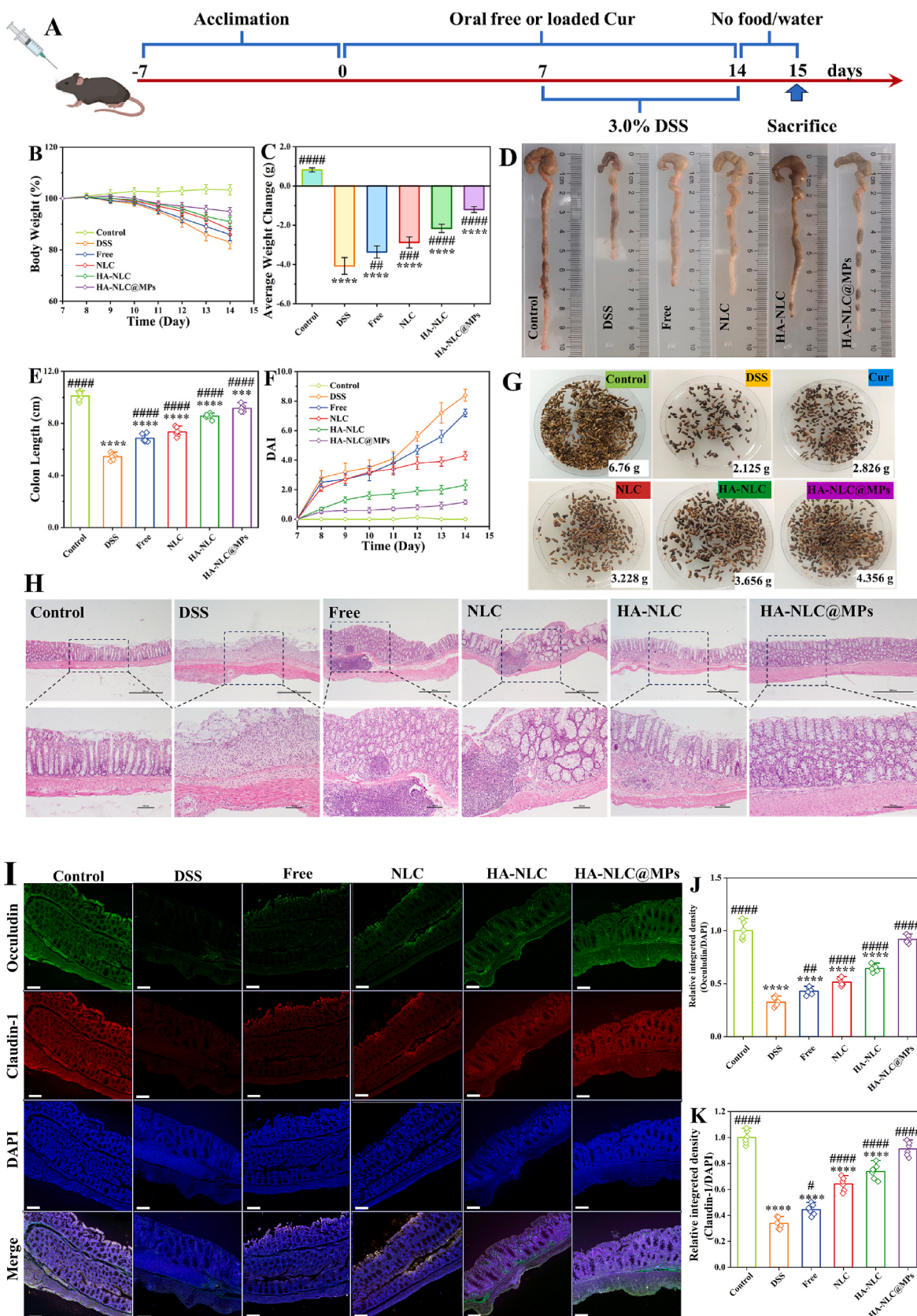


Fig. 6. Therapeutic effects of Cur carriers against the DSS-induced colitis. (A) Schematic illustration of the *in vivo* nutrition intervention of DSS-induced UC in mice by different Cur formulations. (B) Body weight, (C) average weight change, (D) optical photographs of colons, (E) colon length, (F) disease activity index (DAI), (G) optical photographs of feces and (H) H&E staining of the colonic sections. (I) Representative immunofluorescence staining of the tight junction proteins in the colon tissue, and the relative integrated density of (J) occludin and (K) claudin-1 by Image-J software. Bar in H: 500 μ m (upper panel), 100 μ m (lower panel). Bar in I: 100 μ m.

of Ver, indicating that these nanocarriers could effectively overcome the P-gp-mediated efflux and enhance Cur delivery across the monolayers. The size discrepancy made it unfavorable for P-gp to pump the nanocarriers out of the cells (Li et al., 2024). Biopolymer nanoparticles were also found to increase the P-gp-ATPase activity, consequently reducing the intracellular ATP levels and disrupting the energy supply required for P-gp-mediated drug efflux (Xiong et al., 2021).

The anti-inflammatory effects of free and encapsulated Cur were analyzed using a dual-chamber cell model, as illustrated in Fig. 4A. Cur that permeated across the Caco-2 monolayers alleviates the inflammatory responses of the macrophages induced by LPS. Epithelial tight junction proteins, such as claudin and occludin, are essential for maintaining the integrity of the intestinal mechanical barriers. Damage to these proteins allows harmful substances to penetrate the mucosal barrier and results in inflammation (Hu et al., 2020; Tian et al., 2022). Both the immunofluorescence signals of occludin (green) and claudin-1 (red) in the Caco-2 monolayers decreased obviously after LPS treatment (Fig. 4B), indicating severe damage to the intestinal mucosal barrier. All three Cur formulations notably enhanced the expression of the tight junction proteins. As shown in Fig. 4C, the fluorescence intensity of occludin in the free, NLC, and HA-NLC group was 1.19-, 1.47-, and 1.72-fold higher than that in the LPS group, respectively. Moreover, HA-NLC showed the highest efficacy in enhancing claudin-1 expression (Fig. 4D). No significant differences ($p > 0.05$) were observed between the HA-NLC group and the control groups in the levels of both tight junction proteins.

Accordingly, due to the enhanced expression of occludin and claudin-1, the TEER values in the three intervention groups were significantly higher ($p < 0.0001$) than that in the LPS group (Fig. 4E). Cur in HA-NLC was the most effective in improving the TEER value, followed by Cur in NLC and free Cur. The TEER level in the HA-NLC group was very close to that in the control groups. These results suggest that Cur in HA-NLC could more effectively restore normal intestinal barrier function than the other Cur formulations.

Excessive reactive oxygen species (ROS) are closely linked to the inflammatory reaction (Chen et al., 2021). Therefore, developing potent ROS scavengers in proinflammatory immune cells is a strategy for managing local inflammation. The ROS levels in the BL side of the dual-chamber model were assessed using CellROX™ Deep Red, which can be oxidized to produce intense red fluorescence (Fig. 4F). The intensity of the red ROS signal nearly doubled in response to LPS treatment (Fig. 4G). Free Cur reduced the ROS level by 18.28 %, likely due to its ability to scavenge free radicals and regulate various signaling pathways (Tsuda, 2018). The ROS scavenging activity of Cur improved remarkably following nanoencapsulation. The ROS levels in the NLC and HA-NLC groups were only 67.16 % and 54.92 % of that in the LPS group, respectively. Additionally, there were no significant differences ($p > 0.05$) in ROS levels between the HA-NLC group and the control group.

Macrophages polarize into M1-type in response to stimuli like LPS, producing various pro-inflammatory cytokines (Liang et al., 2023). The TNF- α content in the supernatant increased from 4.97 pg/mL (control group) to 50.33 pg/mL (LPS group) (Fig. 4H), and the IL-6 content increased from 21.43 pg/mL (control group) to 65.95 pg/mL (LPS group) (Fig. 4I) after LPS treatment, indicating remarkable inflammatory responses occurred. Cur loaded within HA-NLC exhibited the most pronounced suppressive effects on cytokine production, followed by Cur in NLC and free Cur. These findings suggest a positive correlation between the transcellular absorption capacity and the anti-inflammatory effects of various Cur formulations. It was hypothesized that a greater number of Cur molecules in HA-NLC would transport across the Caco-2 monolayers to alleviate inflammatory stress in macrophages, facilitated by CD44-mediated endocytosis effects (Feng et al., 2025; Xu et al., 2022) (Fig. 4).

3.4. Hierarchical microspheres prolong the retention of loaded agent in colitis mice

Prior to the *in vivo* therapeutic efficacy assessments, a biodistribution assay was conducted to evaluate whether the microspheres could effectively prolong the retention of the loaded agent. Immunofluorescent staining was conducted at first to label the CD44⁺ mucosa cells in the colon sections in colitis mice. The abundance of CD44⁺ cells in the control group was remarkably lower compared with that in the DSS group (Fig. 5A). This finding demonstrated that inflammation has led to the overexpression of the CD44 receptors in the mucosa, in line with a previous report (Xu et al., 2022).

The accumulation of the nutraceuticals in the inflamed intestinal tract, particularly in the colon tissue, is crucial for treating colitis *via* oral administration. The colitis mice were given oral dosages of free or encapsulated IR780 at 0.5 mg/kg, and the fluorescence images were captured and analyzed using the IVIS system at predetermined times intervals. As shown in Fig. 5B and D, there was no significant difference ($p > 0.05$) in the average fluorescence intensity across the four groups after oral gavage for 3.0 h. After 12 h, the HA-NLC@MPs and HA-NLC groups exhibited the highest fluorescence intensity, followed by the NLC group and the free group, with significant differences ($p < 0.05$). By the endpoint (24 h), the differences became more pronounced. The mean fluorescence intensity of the HA-NLC@MPs group was 21.59-fold, 4.09-fold, and 2.14-fold greater than that of the free, NLC, and HA-NLC groups, respectively (Fig. 5D).

After 24 h of intragastric administration, the GIT was harvested for evaluation. The fluorescence images and histograms presented in Fig. 5C and E illustrate a decreasing trend in fluorescence intensity as follows: HA-NLC@MPs > HA-NLC > NLC > free. These findings underscored a superior retention rate of the fluorescent probe in the HA-NLC@MPs in the gut compared with that in the other carriers. The pectin matrix of the HA-NLC@MPs enhanced their intestinal adhesiveness and responsiveness to gut microbes (Fig. 2B), while simultaneously facilitating a controlled release of the loaded agents in the GIT (Fig. 2D). On the other hand, the exposed HA moieties selectively bind to CD44 receptors, which enhanced the retention of the loaded agent in the CD44⁺ mucosa areas (Zhu et al., 2024) and promoted its uptake by the inflamed colonic enterocytes through receptor-mediated endocytosis (Fig. 3) (Xu et al., 2022). The hierarchical microspheres exhibited an enhanced mucus-binding affinity due to the pectin matrix, which facilitates hydrogen bonding and causes the microspheres to adhere to mucus in the upper gastrointestinal tract (Yuan et al., 2022). Consequently, additional time is required to reach the colon. We speculate that the colon-targeted accumulation would be more pronounced if the digestive tract were harvested at a later time point. Taken together, HA-NLC@MPs effectively promoted the accumulation of the loaded agent within the GIT, especially in the inflamed colon, thereby holding great promise in enhancing its nutrition intervention efficacy.

3.5. Cur in HA-NLC@MPs possesses therapeutic effects in DSS-induced colitis

The therapeutic efficacy of orally administered Cur carriers on UC was assessed using a DSS-induced colitis mice model (Fig. 6A). The main clinical parameters evaluated included body weight change, colon length, and the occurrence of bloody stools (Xiao et al., 2018). As depicted in Fig. 6B, the mice in both the DSS and treated groups exhibited gradual weight reduction following the replacement of drinking water with a 3 % DSS solution. Conversely, mice in the control groups showed slight weight gain. By day 14, mice in the DSS group experienced a weight loss of $-4.08 \pm 0.43\%$ (Fig. 6C). Nutritional intervention with free or encapsulated Cur significantly inhibited weight loss ($p < 0.05$). The highest protection effect was observed with Cur in HA-NLC@MPs, showing a weight loss of only $-1.20 \pm 0.15\%$, followed by Cur in HA-NLC ($-2.16 \pm 0.21\%$), Cur in NLC ($-2.88 \pm 0.28\%$), and

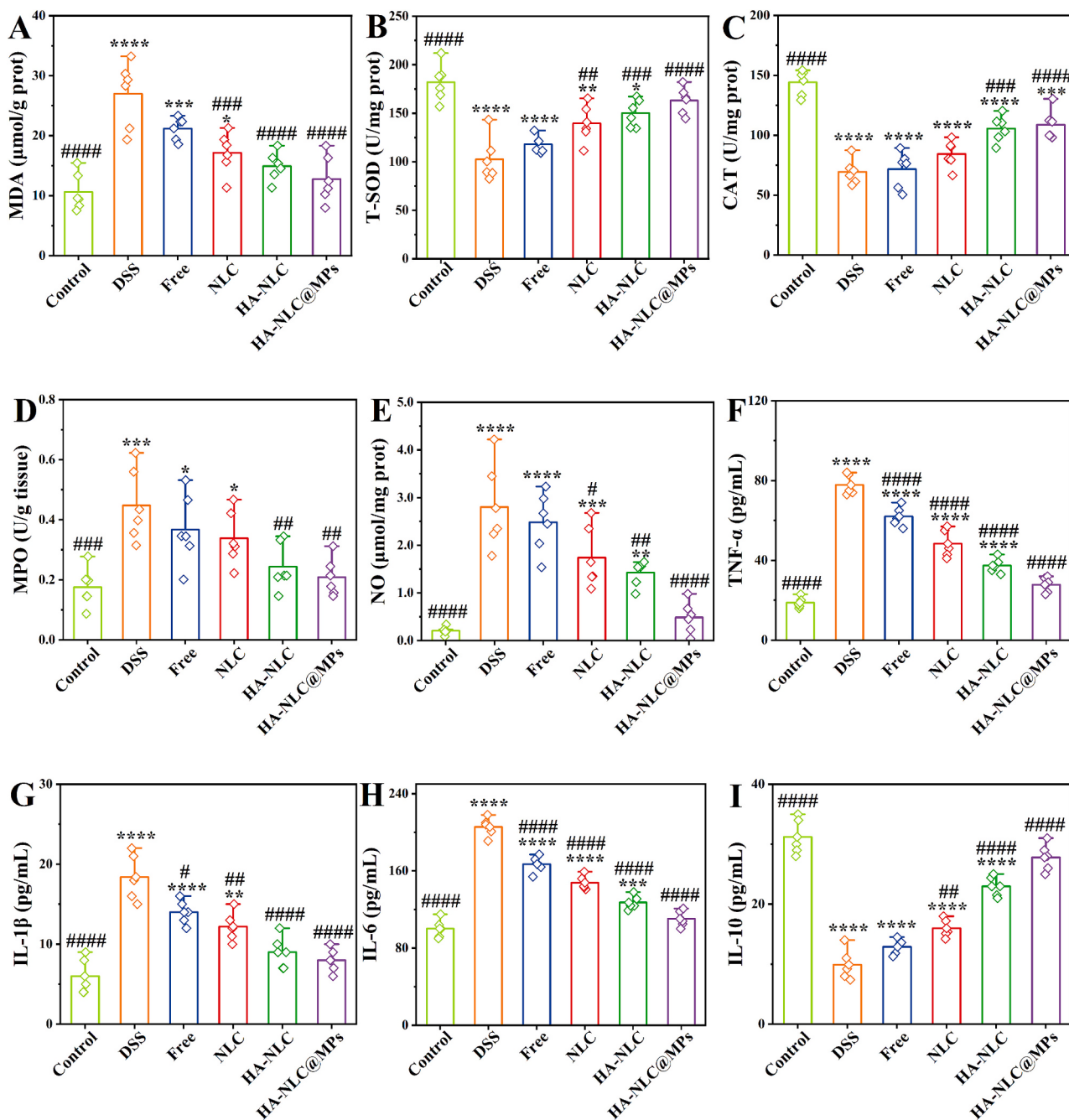


Fig. 7. Effect of orally administered Cur carriers on the oxidative stress and inflammatory cytokine levels in mice with DSS-induced colitis. (A) MDA level, (B) T-SOD activity, (C) CAT activity, (D) MPO activity, (E) NO level, pro-inflammatory cytokines levels of (F) TNF- α , (G) IL-6, and (H) IL-1 β , and anti-inflammatory cytokines level of (I) IL-10 in serum. *, **, ***, and **** represent $p < 0.05$, $p < 0.01$, $p < 0.001$, and $p < 0.0001$, respectively, compared with the control; #, ##, ###, and ##### represent $p < 0.05$, $p < 0.01$, $p < 0.001$, and $p < 0.0001$, respectively, compared with the DSS group.

free Cur ($-3.36 \pm 0.31\%$).

As depicted in Fig. 6D, the colon of the control group was uniformly smooth and free of edema, whereas the colon in the DSS group displayed edema and was shortened. The symptom of colonic shortening was alleviated in the treated groups. Specifically, compared with the DSS group, free, NLC, HA-NLC, and HA-NLC@MPs groups showed colon length increase by 1.26-, 1.35-, 1.57-, and 1.68-fold, respectively (Fig. 6E). Similar trends were observed in the DAI scores. Between day 8 and day 14, the DAI scores of the HA-NLC@MPs group were remarkably lower than those of the free, NLC, and HA-NLC groups (Fig. 6F). UC also leads to a reduction in fecal output in mice, often accompanied by symptoms such as diarrhea and loose stools (Xing et al., 2024). In the

DSS group, the fecal mass at the last day of the experiment was only one-third of that in the control group (Fig. 6G). Treatment with free or encapsulated Cur resulted in an improvement in fecal mass, with the most prominent effects observed in the HA-NLC@MPs group.

Histopathological examination using H&E staining confirmed that the colonic tissues from the control group displayed a dense and intact columnar epithelium, with fully developed intestinal crypts (Fig. 6H). The distinct interface between the mucosal and submucosal layers was clearly visible (Liang et al., 2023). Conversely, in the DSS-treated group, there was remarkable damage to the superficial epithelium and goblet cells, accompanied by extensive infiltration of inflammatory mononuclear leukocytes within the mucosal and submucosal layers.

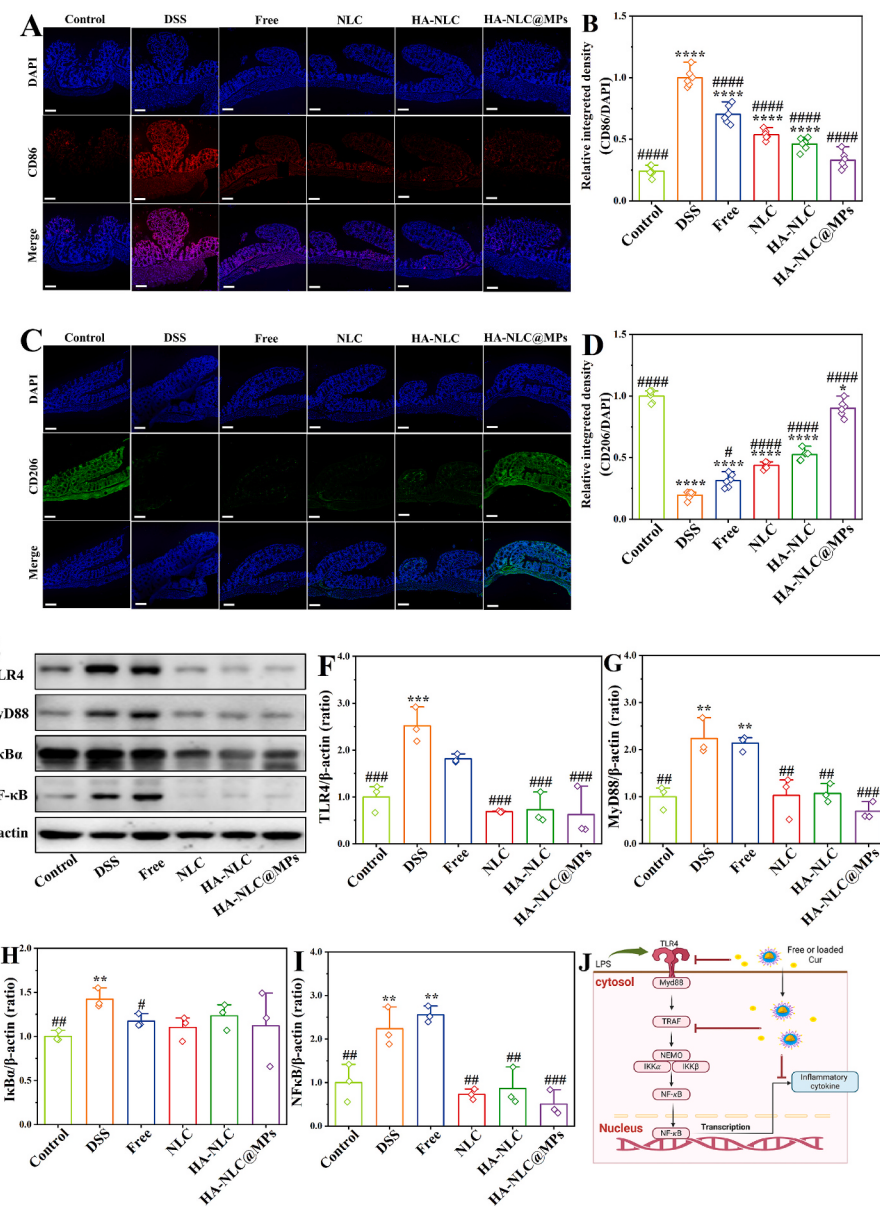


Fig. 8. Regulating effects of various Cur formulations on macrophage polarization and TLR4/MyD88/NF-κB signaling pathways. Immunofluorescence staining of (A) CD86 and (C) CD206 and (B and D) the corresponding semiquantitative analysis results in different groups. (E) Western blot analysis of the TLR4/MyD88/NF-κB signaling cascade and (F–I) the quantitative analysis of the protein expression levels. (J) A schematic diagram illustrating the potential mechanism of Cur intervention on inflammatory cytokine production through this pathway. *, **, ***, and **** represent $p < 0.05$, $p < 0.01$, $p < 0.001$ and $p < 0.0001$, respectively, compared with the control; #, ##, ###, and ##### represent $p < 0.05$, $p < 0.01$, and $p < 0.001$, and $p < 0.0001$, respectively, compared with the DSS group. Bar in A and C: 100 μm.

Furthermore, edematous changes were observed in the interface between the intestinal mucosa and muscular layers (Hu, Yu, Shi, et al., 2020). Moderate recovery from the pathological damage was observed across the free, NLC, and HA-NLC groups, indicated by reduced infiltration of inflammatory cells and decreased edema. Notably, HA-NLC@MPs showed the most significant alleviation, restoring mucus-secreting goblet cell levels to normal, promoting the formation of intact crypts, and eliminating cell infiltration. These collective findings suggested that HA-NLC@MPs effectively ameliorate clinical symptoms in DSS-induced colitis mice.

UC disrupts the intestinal epithelial barrier and promotes bacterial translocation and the entry of other antigens (Cao et al., 2021). The expressions of tight junction proteins in colonic tissue were further analyzed by immunofluorescence (Fig. 6I–K). DSS treatment significantly ($P < 0.05$) reduced the levels of occludin and claudin-1, with

fluorescence intensities measuring only 32.45 % (Fig. 6J) and 33.84 % (Fig. 6K) of those in the control groups, respectively, indicating severe disruption of the intestinal barriers. The free Cur group showed a modest improvement in protein expression levels. NLC encapsulation enhanced the barrier function restoration effects of Cur by improving its intestinal absorption (Fig. 3F) and bioaccessibility (Li et al., 2022). In the HA-NLC group, the levels of the tested proteins reached approximately 70 % of normal levels owing to the CD44 receptor-mediated Cur absorption. The most pronounced mucosa-protecting effects were observed in the HA-NLC@MPs group, which showed no significant differences ($p > 0.05$) in barrier protein levels when comparing with the control group (Fig. 6J and K).

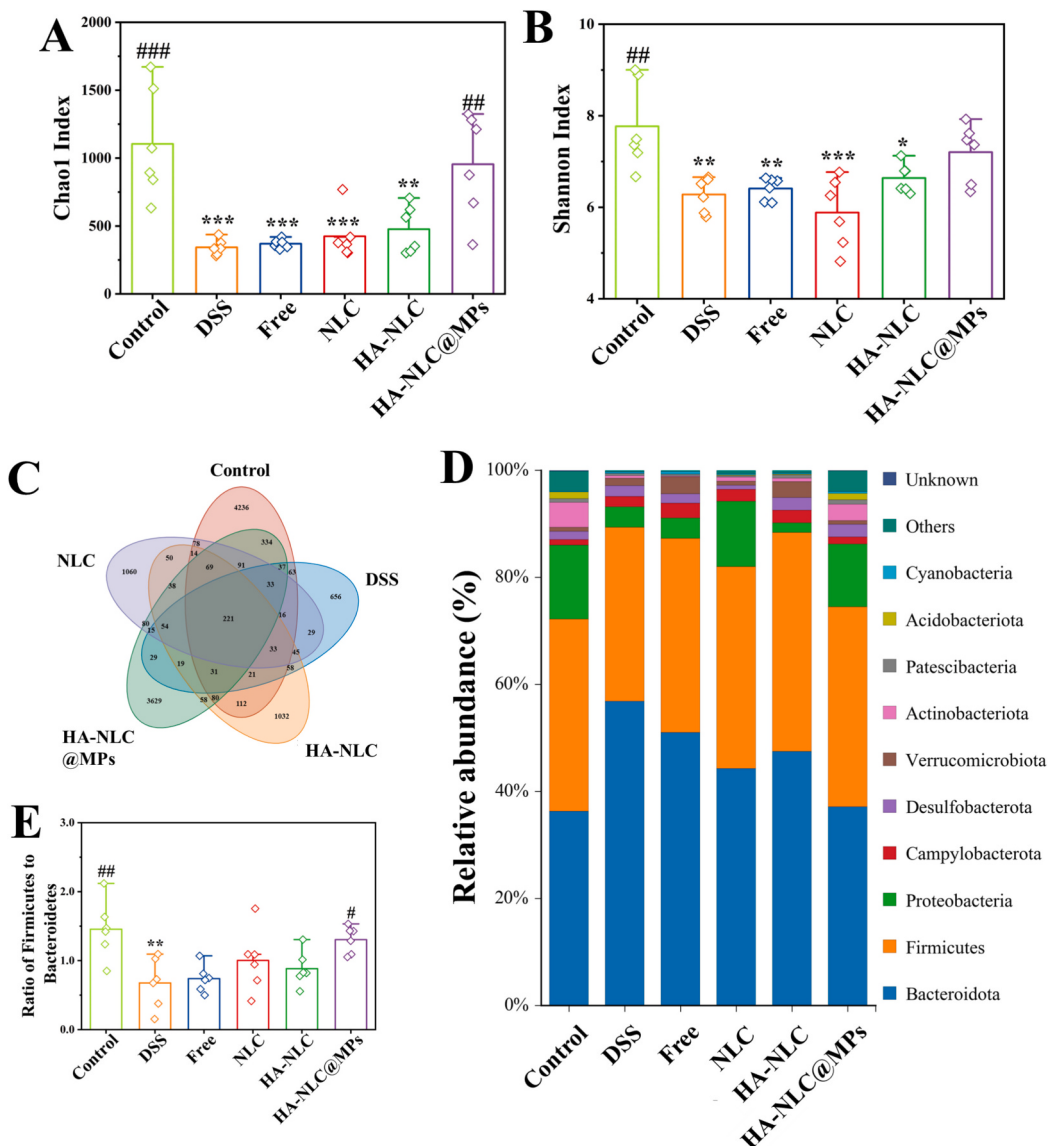


Fig. 9. (A) Gut microbiota index and (B) Shannon index of OTU level analysis in different groups. (C) Venn diagram of shared and unique bacteria at OTU level. (D) Gut microbiota composition at phylum level and (E) the ratio of *Firmicutes* to *Bacteroidetes*.

3.6. Cur in HA-NLC@MPs attenuates oxidative and inflammatory stress *in vivo*

This section assesses the effect of various Cur formulations on oxidative and inflammatory stresses in colitis mice. Free Cur exhibited a modest reduction in MDA level (Fig. 7A), a marker of peroxidation status, relative to the DSS group; however, this effect was not statistically significant ($p > 0.05$). Enhanced therapeutic effects were observed with the encapsulated Cur, as both Cur in HA-NLC and HA-NLC@MPs restored MDA level to the normal state ($p > 0.05$ compared with the control group). Similar trends were observed for the activities of anti-oxidant enzymes such as T-SOD (Fig. 7B) and CAT (Fig. 7C). These findings suggested that Cur in HA-NLC and HA-NLC@MPs effectively alleviate oxidative stress *in vivo*. MPO (Fig. 7D) and NO (Fig. 7E) in colon tissues are closely linked to the onset of inflammation (Liang et al., 2023). The levels of MPO and NO in the HA-NLC@MPs group decreased by 53.40 % and 82.70 %, respectively, compared with the DSS group, making the lowest values among the four treated groups.

The production of both pro-inflammatory and anti-inflammatory cytokines is closely linked to colon injury during the progression of

colitis (Xu et al., 2022). Results indicated that treatment with various Cur formulations led to significant ($p < 0.05$) reductions in the levels of pro-inflammatory cytokines TNF- α (Fig. 7F), IL-1 β (Fig. 7G), and IL-6 (Fig. 7H). The serum IL-10 level in the DSS group was only one-third of that in the control group, and it showed an increase following treatment with various Cur formulations (Fig. 7I). Among the four treatment groups, Cur in HA-NLC@MPs demonstrated greater efficacy in suppressing the expression of pro-inflammatory cytokines and promoting the expression of anti-inflammatory cytokine. Notably, there were no significant differences ($p > 0.05$) in these cytokine levels between the HA-NLC@MPs group and the control group. In summary, the *in vivo* studies indicated that Cur in HA-NLC@MPs demonstrated exceptional anti-inflammatory effects, primarily due to the carrier's ability to deliver Cur to the inflamed colon tissues.

3.7. Cur in HA-NLC@MPs modulates macrophage polarization and TLR4/MyD88/NF- κ B signaling cascade

Mechanisms underlying the anti-colitis capacity of Cur in HA-NLC@MPs were further elucidated. The polarization dynamics of

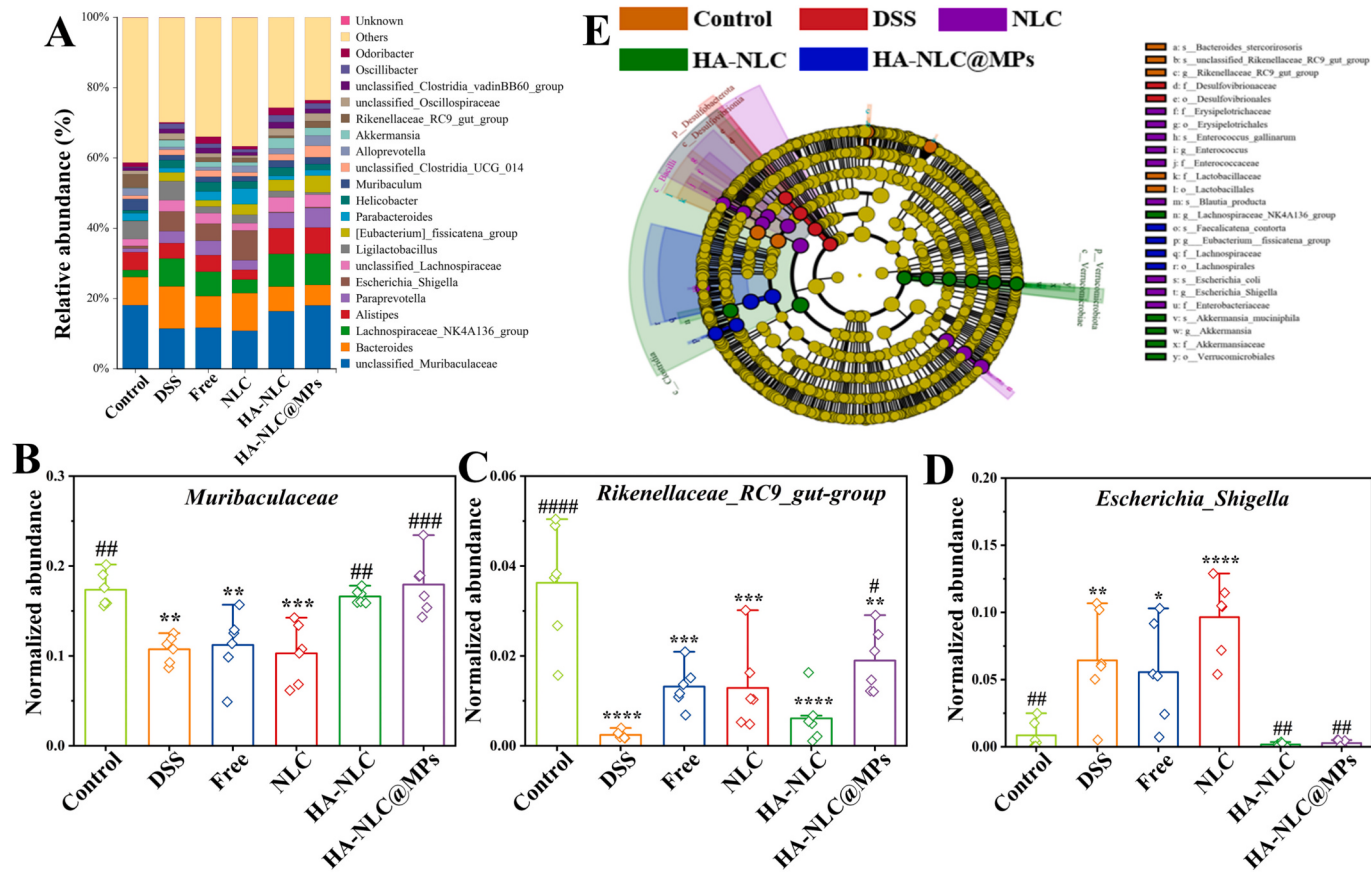


Fig. 10. (A) Gut microbiota composition at Genus level. Normalized abundance of (B) *Muribaculaceae*, (C) *Rikenellaceae_RC9_gut-group*, and (D) *Escherichia_Shigella*. (E) LEfSe analysis of the gut microbiota in control, DSS, NLC, HA-NLC, and HA-NLC@MPs groups.

macrophage within colonic tissues were examined at first (Fig. 8A-D). TNF- α , IL-6, and IL-1 β are secreted by M1 macrophages, while IL-10 is secreted by M2 macrophages (Li, Zhu, et al., 2024). Therefore, modulating the phenotypic shifts of macrophages from M1 to the M2 state is pivotal for enhancing the therapeutic effects in colitis. Compared with the control group, the DSS group displayed an augmented M1 phenotype, evidenced by heightened CD86 expression (Fig. 8A and B), and a diminished M2 phenotype, indicated by lower CD206 expression (Fig. 8C and D), reflecting exacerbated inflammatory states. Free Cur or Cur delivered via NLC, HA-NLC and HA-NLC@MPs effectively reversed this trend, resulting in a marked decrease in CD86 expression and a corresponding increase in CD206 expression. Of particular interest, the HA-NLC@MPs formulation exhibited the most pronounced effects. Notably, there were no significant differences ($p > 0.05$) observed in CD86 level between the control group and the HA-NLC@MPs group (Fig. 8B).

TLR4 is a key pattern recognition receptor predominantly found on macrophages. Upon binding to its ligands, TLR4 interacts with MyD88 to trigger the NF- κ B signaling pathway. The activation of this pathway leads to the translocation of the cytoplasmic transcription factor NF- κ B into the nucleus, where it binds to DNA and orchestrates the transcription of pro-inflammatory genes (Tie et al., 2022). According to the Western blot results (Fig. 8E) and protein expression analysis (Fig. 8F-I), DSS pretreatment significantly upregulated the expression of TLR4 ($p < 0.001$), MyD88 ($p < 0.01$), I κ B α ($p < 0.01$), and NF κ B ($p < 0.01$), indicating the activation of the TLR4/MyD88/NF- κ B signaling pathways. By contrast, Cur, particularly when delivered through various carriers, substantially attenuates these increases. As illustrated in Fig. 8J, the modulation of this signaling cascade inhibits the secretion of inflammatory cytokines and slows the progression of colitis.

3.8. Cur in HA-NLC@MPs reshapes the gut microbiota homeostasis

Colitis progression is closely associated with the dysbiosis of gut microbiota. Given the condition that the HA-NLC@PMs facilitated the colonic delivery of encapsulated Cur (Figs. 2 and 5), this formulation was also hypothesized to reshape the gut microbiota in colitis mice. Herein, 16S rDNA amplicon sequencing was employed to analyze the composition and relative abundance of the microbial communities. The numbers, species richness, and uniformity of sequenced samples were suitably consistent across various groups, as indicated by the rarefaction curves (Fig. S6A) and rank abundance analysis (Fig. S6B). As illustrated by the species accumulation boxplot in Fig. S6C, the number of species reached an asymptotical stability with an increase in sample numbers, and the diversity in the samples decreased. This result indicated that the sequencing depth was sufficiently comprehensive to accurately represent the composition of the gut microbiota (Liang et al., 2023).

The α -diversity, as measured by Chao 1 or Shannon indices, was significantly depressed in the DSS-treated groups compared with the control group (Fig. 9A and B). Through free Cur and Cur encapsulated in NLC and HA-NLC could improve the Chao 1 index in colitis mice, these enhancements were not statistically significant ($p > 0.05$) (Fig. 9A). By contrast, Cur in HA-NLC@MPs could significantly ($p < 0.01$) increase the Chao 1 index in colitis mice. On the other hand, neither free nor encapsulated Cur elicited a significant improvement on the Shannon index (Fig. 9B). The Venn diagram depicted in Fig. 9C highlighted that, despite sharing 221 operational taxonomic units (OTUs), the unique species varied substantially among the groups. The numbers of special OTUs in the control, DSS, NLC, HA-NLC, and HA-NLC@MPs groups were 4236, 656, 1060, 1032, and 3629, respectively. The qualitative differences in the gut microbiota were found to exert a more profound impact

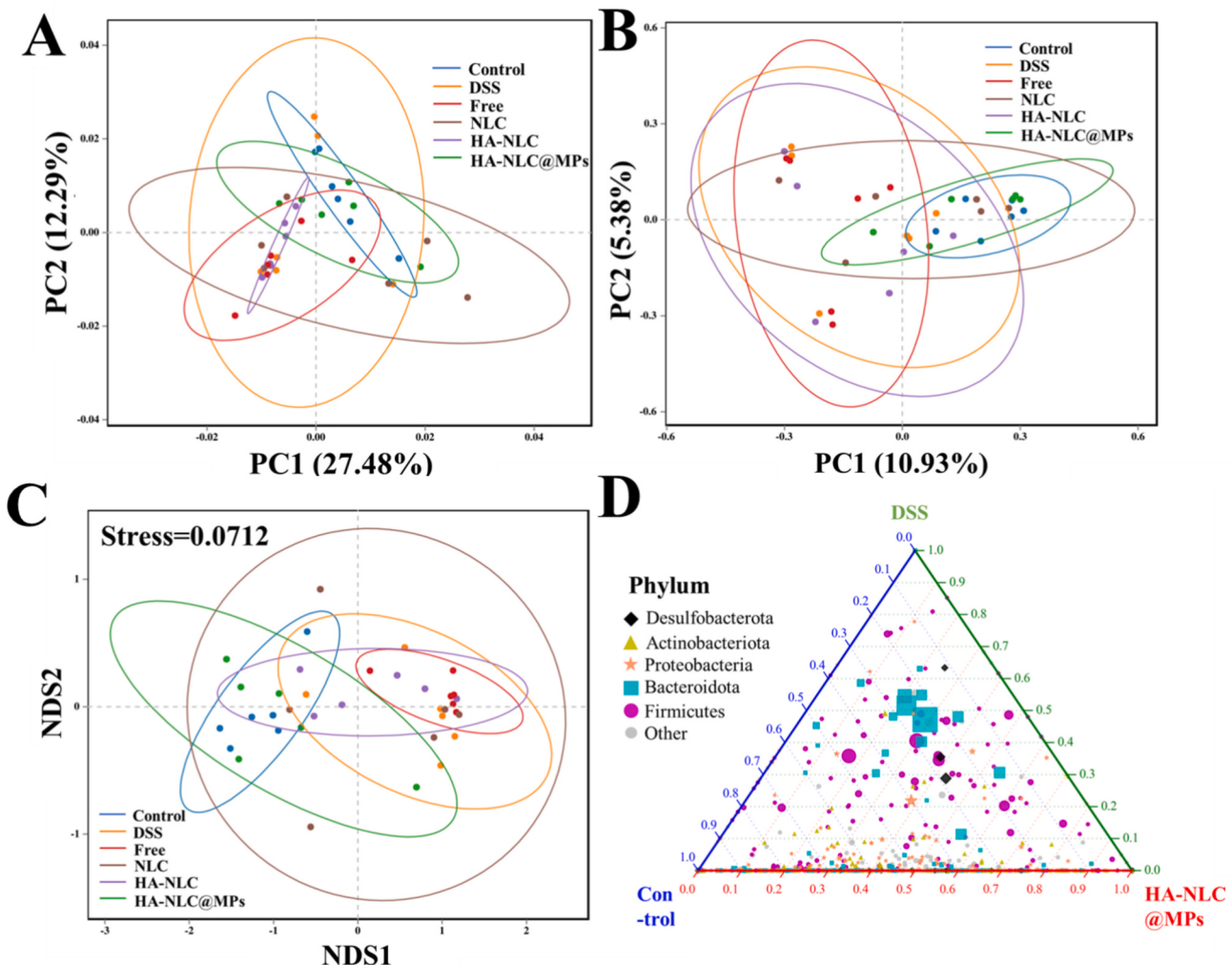


Fig. 11. (A) PCA, (B) PCoA, and (C) NMDS analysis of the gut microbiota. (D) Ternary analysis of the composition of core microbiota at phylum level in control, DSS, and HA-NLC@MPs groups.

on gut homeostasis than purely quantitative discrepancies (Wang et al., 2022).

The results from the gut microbiota at the phylum level elucidated that Firmicutes and Bacteroidetes constitute the predominant microbiota across all groups (Fig. 9D). Notably, the ratio of Firmicutes to Bacteroidetes in the DSS-treated groups was significantly diminished ($p < 0.05$) relative to the control group (Fig. 9E). This result aligns with the activation of inflammatory responses, as corroborated by previous studies (Li, Zhu, et al., 2024; Liang et al., 2023). Both free and encapsulated Cur were capable of reversing this trend; however, only Cur encapsulated in HA-NLC@MPs demonstrated a significant improvement ($p < 0.05$ compared with the DSS group). Additionally, Cur in HA-NLC@MPs reduced the relative abundance of harmful bacteria, such as Campylobacterota.

As illustrated in Fig. 10A and Fig. S7, family *Muribaculaceae*, genus *Alistipes*, *Muribaculum*, and the *Rikenellaceae_RC9_gut-group* are notably abundant in the control group. Both *Muribaculaceae* and *Muribaculum* have demonstrated the capacity to mitigate severe mucosal injury in colitis mice by competitively restricting the proliferation of a variety of pathogenic bacteria, including *Clostridium difficile*, which facilitates goblet cell differentiation and enhances the expression of tight junction proteins (Pereira et al., 2020). *Alistipes* and the *Rikenellaceae_RC9_gut-group* contributed to the production of SCFAs (Tie et al., 2022). DSS treatment significantly ($p < 0.05$) decreased the abundance of

Muribaculaceae (Fig. 10B) and *Rikenellaceae_RC9_gut-group* (Fig. 10C), whereas increased the abundance of *Escherichia_Shigella* (Fig. 10D), which has been reported to disrupt the mucus layer and enhance the infection by pathogenic bacteria (Wang et al., 2022). Compared with the free, NLC, and HA-NLC groups, Cur in HA-NLC@MPs were more effective in promoting the abundance of *Muribaculaceae* (Fig. 10A and B) and the *Rikenellaceae_RC9_gut-group* (Fig. 10A and C), while simultaneously inhibiting the growth of *Escherichia_Shigella* (Fig. 10A and D).

Linear discriminant analysis effect size (LEfSe) is an analytical tool to discover and interpret microbial biomarkers, enabling the identification of species with statistically significant differences among various groups (Fig. 10E). The relative abundance of the family *lachnospiraceae*, a biomarker associated with the HA-NLC@MPs group, was observed to be remarkably higher compared with the other groups. This family holds the potential to alleviate the DSS-induced colitis by elevating the levels of SCFAs (Wang et al., 2022).

The microbial heatmap at the taxonomic levels of phylum (Fig. S8A) and genus (Fig. S8B) revealed that the control group and the Cur in HA-NLC@MPs group were tightly clustered, clearly distinguishing them from the DSS group. This clustering pattern emphasized that the gut microbiota composition in the HA-NLC@MPs group closely resembles that of healthy mice. In-depth diversity analyses, encompassing principal component analysis (PCA) (Fig. 11A) and principal coordinate analysis (PCoA) analysis (Fig. 11B), further corroborated this

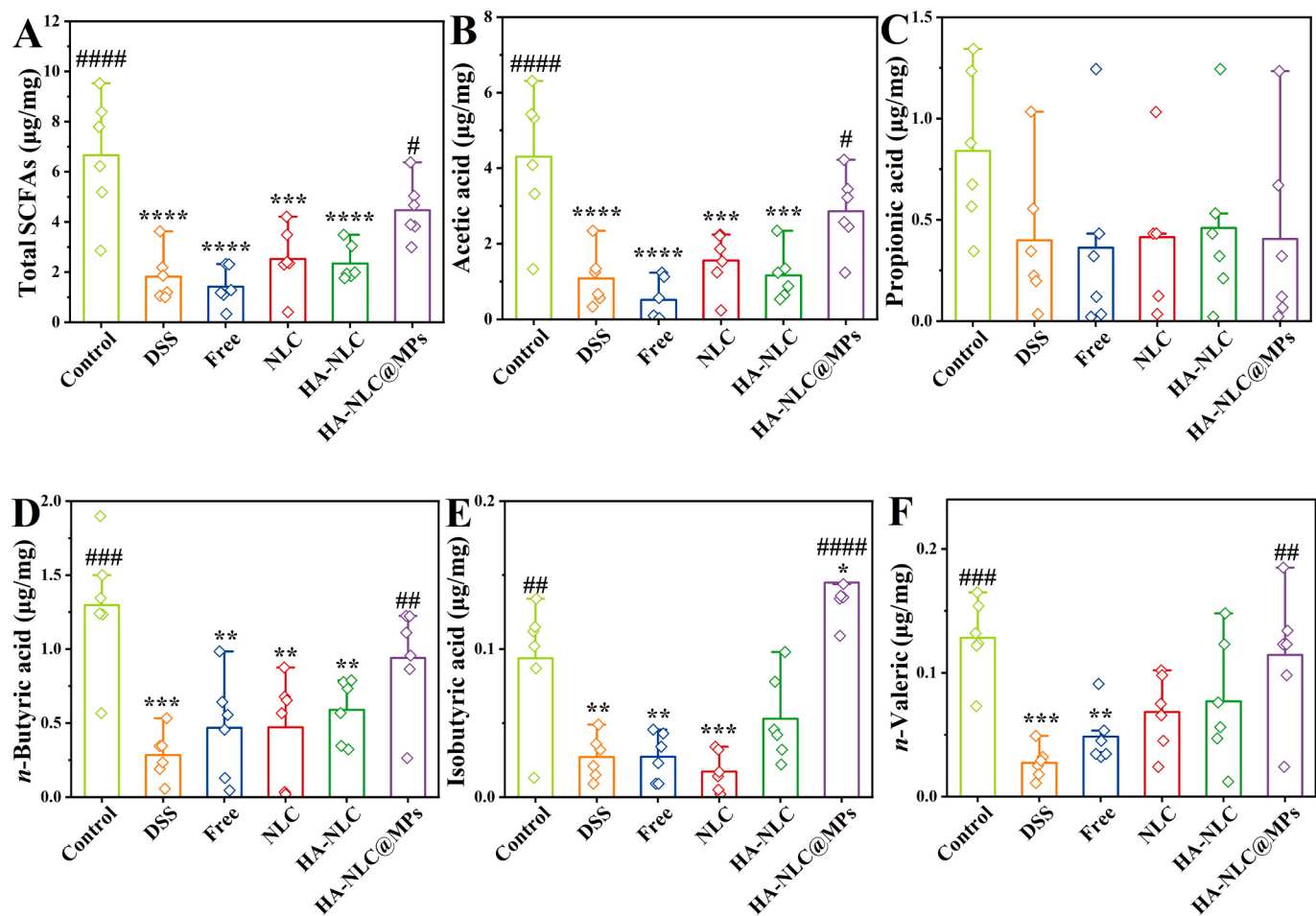


Fig. 12. Enrichment of SCFAs in cecum by Cur in HA-NLC@MPs. (A) Total SCFAs, (B) acetic acid, (C) propionic acid, (D) *n*-butyric acid, (E) isobutyric acid, and (F) *n*-valeric acid levels. *, **, ***, and **** represent $p < 0.05$, $p < 0.01$, $p < 0.001$, and $p < 0.0001$, respectively, compared with the control group; #, ##, ###, and ##### represent $p < 0.05$, $p < 0.01$, $p < 0.001$, and $p < 0.0001$, respectively, compared with the DSS group.

observation. These analyses indicated that the distance between the control group and the HA-NLC@MPs group was minimal, underscoring their highly similarity in microbial community composition. By contrast, the other three treated groups demonstrated a markedly more dispersed distribution, or a high distance from the control group. The findings from non-metric multidimensional scaling (NMDS) analysis, with stress value below 0.1, further validated these observations (Fig. 11C). The close resemblance between these two groups highlighted the efficacy of Cur in HA-NLC@MPs in restoring a near-physiological microbial architecture through targeted colon accumulation. The ternary phase evaluation of core microbiota at the phylum level (Fig. 11D) indicated that the overall species abundance in the HA-NLC@MPs group closely matched that of the control group but differed from the DSS group.

3.9. Cur in HA-NLC@MPs improves the levels of SCFAs

Gut microbiota modulates its biological effects on the host by producing various microbial products, with SCFAs being particularly implicated in the pathogenesis of colitis. SCFAs have been reported to enhance the population and functionality of the regulatory T cells, which consequently promote the restoration of tight junction protein expression and alleviate colitis (Hu, Yu, Shi, et al., 2020). In the DSS group, the level of total SCFAs was approximately one-third of that in the control group ($p < 0.0001$). Treatment with Cur encapsulated in HA-NLC@MPs significantly ($p < 0.05$ compared with DSS group) elevated the SCFAs to a level comparable with that of the control group (Fig. 12A). This enhancement was primarily attributed to the increased

levels of acetic acid (Fig. 12B), the most abundant SCFAs. Additionally, Cur in HA-NLC@MPs also significantly ($p < 0.05$ compared with DSS group) improved the levels of *n*-butyric acid (Fig. 12D), isobutyric acid (Fig. 12E), and *n*-valeric acid (Fig. 12F). Free Cur or Cur in NLC and HA-NLC, which facilitated Cur accumulation in the upper GIT, also made contributions to the elevation of acetic acid, *n*-butyric acid, isobutyric acid, and *n*-valeric acid. However, these effects were statistically insignificant ($p > 0.05$). No significant differences were observed in the levels of propionic acid among the control, DSS, and treated groups (Fig. 12C).

3.10. The Cur carriers exhibited superb compatibility and biosafety

Following extensive investigations into the therapeutic efficacy of Cur delivery systems for managing colitis and elucidating the related mechanisms, it imperative to assess their long-term safety profiles. Oral administration of Cur encapsulated in NLC, HA-NLC, and HA-NLC@MPs over an 8-week period did not induce any observable damage to vital organs including hearts, livers, spleens, lungs, kidneys and testicles (Fig. S9). Furthermore, there was no significant elevations ($p > 0.05$) in the key serum biochemistry indices such as ALT (Fig. S10A), AST (Fig. S10B), TBIL (Fig. S10C), Crea (Fig. S10D), urea (Fig. S10E), BUN (Fig. S10F), T-CHO (Fig. S10G), and TG (Fig. S10H) at the end of the test. All these indices remained within the standard physiological range. These findings unequivocally demonstrated the exceptional biocompatibility of these Cur delivery systems, revealing their potential for both therapeutic and nutritional interventions.

4. Conclusions

The designation of targeted delivery vehicles with predictable gastrointestinal fate and enhanced absorption/metabolite outcomes can be achieved through strategic material selection and structure engineering. The hierarchical system HA-NLC@MPs with sequence-targeted capability were demonstrated to augment Cur accumulation specifically in the inflamed colon area. The pectin matrix effectively prevented Cur leakage in the upper GIT and was degraded by microbiota in colon. Following that, the Cur-loaded HA-NLC, released from the microspheres, was absorbed by the inflamed colonic enterocytes through receptor-mediated endocytosis, primarily driven by the specific interactions between the over-expressed CD44 receptors and the HA moieties. Compared with free Cur, Cur in NLC, and Cur in HA-NLC, Cur in HA-NLC@MPs demonstrated superior therapeutic effects in DSS-induced colitis, which included repairing intestinal injury, enhancing barrier function, and attenuating oxidative and inflammatory stress. The anti-colitis mechanisms encompassed the phenotypic shifts of macrophages from M1 to M2 state, the inactivation of the TLR4/MyD88/NF- κ B pathway, and the proliferation of the mucus-associated *Muribaculaceae* and SCFAs-producing *Rikenellaceae_RC9_gut-group* and *lachnospiraceae*. By contrast, when encapsulated in NLC or HA-NLC, Cur demonstrated accumulation in the upper GIT, and its anti-colitis effects were primarily associated with the TLR4/MyD88/NF- κ B pathway. These observations indicated that altering the core agents' accumulation sites through strategic structural modifications can potentially shift the mechanisms of their bio-efficacy. This study emphasized the potential of hierarchical microspheres for targeted delivery of nutraceuticals to the distal gut with enhanced nutrition intervention efficacy.

CRediT authorship contribution statement

Jin Feng: Writing – review & editing, Project administration, Investigation, Funding acquisition, Conceptualization. **Zhen Wang:** Writing – original draft, Investigation. **Xingyu Zhao:** Formal analysis, Data curation. **Lujing Xu:** Investigation. **Cong Teng:** Visualization. **Songbai Liu:** Resources. **Wuyang Huang:** Supervision, Methodology. **Ying Li:** Project administration, Funding acquisition.

Declaration of competing interest

The authors state that they have no known competing financial interests or personal relationships that could have influenced the work reported in this paper.

Acknowledgements

This work was supported by the National Natural Science Foundation of China (31801555), the Natural Science Foundation of Jiangsu Province (BK20180298), and the Independent Innovation Fund of Agricultural Science and Technology in Jiangsu Province (CX(24)3040).

Appendix A. Supplementary data

Supplementary data to this article can be found online at <https://doi.org/10.1016/j.carbpol.2025.123273>.

Data availability

Data will be made available on request.

References

- Aguilera-Garrido, A., del Castillo-Santaella, T., Galisteo-González, F., José Gálvez-Ruiz, M., & Maldonado-Valderrama, J. (2021). Investigating the role of hyaluronic acid in improving curcumin bioaccessibility from nanoemulsions. *Food Chemistry*, 351, Article 129301. <https://doi.org/10.1016/j.foodchem.2021.129301>
- Akbari-Alavijeh, S., Shaddel, R., & Jafari, S. M. (2020). Encapsulation of food bioactives and nutraceuticals by various chitosan-based nanocarriers. *Food Hydrocolloids*, 105, Article 105774. <https://doi.org/10.1016/j.foodhyd.2020.105774>
- Ban, C., Jo, M., Park, Y. H., Kim, J. H., Han, J. Y., Lee, K. W., ... Choi, Y. J. (2020). Enhancing the oral bioavailability of curcumin using solid lipid nanoparticles. *Food Chemistry*, 302, Article 125328. <https://doi.org/10.1016/j.foodchem.2019.125328>
- Bao, C., Liu, B., Li, B., Chai, J., Zhang, L., Jiao, L., ... Li, Y. (2020). Enhanced transport of shape and rigidity-tuned α -lactalbumin nanotubes across intestinal mucus and cellular barriers. *Nano Letters*, 20(2), 1352–1361. <https://doi.org/10.1021/acs.nanolett.9b04841>
- Cao, Y., Gao, J., Zhang, L., Qin, N., Zhu, B., & Xia, X. (2021). Jellyfish skin polysaccharides enhance intestinal barrier function and modulate the gut microbiota in mice with DSS-induced colitis. *Food & Function*, 12(20), 10121–10135. <https://doi.org/10.1039/DFOO2001C>
- Chen, S., Zheng, J., Zhang, L., Cheng, H., Orfilla, C., Ye, X., & Chen, J. (2021). Synergistic gelling mechanism of RG-I rich citrus pectic polysaccharide at different esterification degrees in calcium-induced gelation. *Food Chemistry*, 350, Article 129177. <https://doi.org/10.1016/j.foodchem.2021.129177>
- Chen, X., Zhu, X., Gong, Y., Yuan, G., Cen, J., Lie, Q., ... Liu, J. (2021). Porous selenium nanzymes targeted scavenging ROS synchronize therapy local inflammation and sepsis injury. *Applied Materials Today*, 22, Article 100929. <https://doi.org/10.1016/j.apmt.2020.100929>
- Chen, Y., Su, W., Tie, S., Cui, W., Yu, X., Zhang, L., ... Tan, M. (2023). Orally deliverable sequence-targeted astaxanthin nanoparticles for colitis alleviation. *Biomaterials*, 293, Article 121976. <https://doi.org/10.1016/j.biomaterials.2022.121976>
- de Vos, W. M., Tilg, H., Van Hul, M., & Cani, P. D. (2022). Gut microbiome and health: Mechanistic insights. *Gut*, 71(5), 1020–1032. <https://doi.org/10.1136/gutjnl-2021-326789>
- Esfanjani, A. F., Assadpour, E., & Jafari, S. M. (2018). Improving the bioavailability of phenolic compounds by loading them within lipid-based nanocarriers. *Trends in Food Science & Technology*, 76, 56–66. <https://doi.org/10.1016/j.tifs.2018.04.002>
- Feng, J., Huang, M., Chai, Z., Li, C., Huang, W., Cui, L., & Li, Y. (2020). The influence of oil composition on the transformation, bioaccessibility, and intestinal absorption of curcumin in nanostructured lipid carriers. *Food & Function*, 11(6), 5223–5239. <https://doi.org/10.1039/d0fo00473a>
- Feng, J., Wang, Z., Huang, W., Zhao, X., Xu, L., Teng, C., & Li, Y. (2025). Hyaluronic acid-decorated lipid nanocarriers as novel vehicles for curcumin: Improved stability, cellular absorption, and anti-inflammatory effects. *Food Chemistry*, 463, Article 141420. <https://doi.org/10.1016/j.foodchem.2024.141420>
- Hossen, S., Hossain, M. K., Basher, M. K., Mia, M. N. H., Rahman, M. T., & Uddin, M. J. (2019). Smart nanocarrier-based drug delivery systems for cancer therapy and toxicity studies: A review. *Journal of Advanced Research*, 15, 1–18. <https://doi.org/10.1016/j.jare.2018.06.005>
- Hu, B., Yu, S., Shi, C., Gu, J., Shao, Y., Chen, Q., ... Mezzenga, R. (2020). Amyloid-polyphenol hybrid nanofilaments mitigate colitis and regulate gut microbial dysbiosis. *ACS Nano*, 14(3), 2760–2776. <https://doi.org/10.1021/acsnano.9b09125>
- Hu, X., Yu, Q., Hou, K., Ding, X., Chen, Y., Xie, J., ... Xie, M. (2020). Regulatory effects of Ganoderma atrum polysaccharides on LPS-induced inflammatory macrophages model and intestinal-like Caco-2/macrophages co-culture inflammation model. *Food and Chemical Toxicology*, 140, Article 111321. <https://doi.org/10.1016/j.fct.2020.111321>
- Jiang, T., & Charcosset, C. (2022). Encapsulation of curcumin within oil-in-water emulsions prepared by premix membrane emulsification: Impact of droplet size and carrier oil on the chemical stability of curcumin. *Food Research International*, 157, Article 111475. <https://doi.org/10.1016/j.foodres.2022.111475>
- Li, C. Y., Liu, D., Huang, M. G., Huang, W. Y., Li, Y., & Feng, J. (2022). Interfacial engineering strategy to improve the stabilizing effect of curcumin-loaded nanostructured lipid carriers. *Food Hydrocolloids*, 127, Article 107552. <https://doi.org/10.1016/j.foodhyd.2022.107552>
- Li, X., Jafari, S. M., Zhou, F., Hong, H., Jia, X., Mei, X., ... Li, Y. (2023). The intracellular fate and transport mechanism of shape, size and rigidity varied nanocarriers for understanding their oral delivery efficiency. *Biomaterials*, 294, Article 121995. <https://doi.org/10.1016/j.biomaterials.2023.121995>
- Li, Y., Mao, M., Yuan, X., Zhao, J., Ma, L., Chen, F., ... Ji, J. (2024). Natural gastrointestinal stable pea albumin nanomicelles for capsaicin delivery and their effects for enhanced mucus permeability at small intestine. *Biomaterials Research*, 28, 0065. <https://doi.org/10.34133/bmr.0065>
- Li, Y., Zhu, B., Chen, T., Chen, L., Wu, D., Wang, X., ... Hu, J. (2024). Glutathione-responsive nanoplates trigger gaseous intervention of intestinal inflammation through TLR4/MD2/MyD88/NF- κ B/iNOS pathway activation and gut microbiota modulation. *Chemical Engineering Journal*, 493, Article 152849. <https://doi.org/10.1016/j.cej.2024.152849>
- Liang, D., Liu, C., Li, Y., Wu, C., Chen, Y., Tan, M., & Su, W. (2023). Engineering fucoxanthin-loaded probiotics' membrane vesicles for the dietary intervention of colitis. *Biomaterials*, 297, Article 122107. <https://doi.org/10.1016/j.biomaterials.2023.122107>
- Lu, Y., Wu, L., Lin, M., Bao, X., Zhong, H., Ke, P., ... Han, M. (2023). Double layer spherical nanoparticles with hyaluronic acid coating to enhance oral delivery of exenatide in T2DM rats. *European Journal of Pharmaceutics and Biopharmaceutics*, 191, 205–218. <https://doi.org/10.1016/j.ejpb.2023.09.003>
- Luo, R., Lin, M., Fu, C., Zhang, J., Chen, Q., Zhang, C., ... Gao, F. (2021). Calcium pectinate and hyaluronic acid modified lactoferrin nanoparticles loaded rhein with dual-targeting for ulcerative colitis treatment. *Carbohydrate Polymers*, 263, Article 117998. <https://doi.org/10.1016/j.carbpol.2021.117998>
- McClements, D. J. (2020). Advances in nanoparticle and microparticle delivery systems for increasing the dispersibility, stability, and bioactivity of phytochemicals.

- Biotechnology Advances*, 38, Article 107287. <https://doi.org/10.1016/j.biotechadv.2018.08.004>
- Naeem, M., Awan, U. A., Subhan, F., Cao, J., Hlaing, S. P., Lee, J., ... Yoo, J.-W. (2020). Advances in colon-targeted nano-drug delivery systems: Challenges and solutions. *Archives of Pharmacal Research*, 43(1), 153–169. <https://doi.org/10.1007/s12272-020-01219-0>
- Pereira, F. C., Wasmund, K., Cobankovic, I., Jehmlich, N., Herbold, C. W., Lee, K. S., ... Berry, D. (2020). Rational design of a microbial consortium of mucosal sugar utilizers reduces Clostridioides difficile colonization. *Nature Communications*, 11(1), 5104. <https://doi.org/10.1038/s41467-020-18928-1>
- Sabet, S., Rashidinejad, A., Melton, L. D., & McGillivray, D. J. (2021). Recent advances to improve curcumin oral bioavailability. *Trends in Food Science & Technology*, 110, 253–266. <https://doi.org/10.1016/j.tifs.2021.02.006>
- Salminen, H., Helgason, T., Kristinsson, B., Kristbergsson, K., & Weiss, J. (2017). Tuning of shell thickness of solid lipid particles impacts the chemical stability of encapsulated ω -3 fish oil. *Journal of Colloid and Interface Science*, 490, 207–216. <https://doi.org/10.1016/j.jcis.2016.11.063>
- Spinozzi, F., Moretti, P., Perinelli, D. R., Corucci, G., Piergiovanni, P., Amenitsch, H., ... Blasi, P. (2024). Small-angle X-ray scattering unveils the internal structure of lipid nanoparticles. *Journal of Colloid and Interface Science*, 662, 446–459. <https://doi.org/10.1016/j.jcis.2024.02.076>
- Tan, C., Yao, X., Jafari, S. M., Sun, B., & Wang, J. (2023). Hyaluronic acid-based nanodelivery systems for food bioactive compounds. *Trends in Food Science & Technology*, 141, Article 104163. <https://doi.org/10.1016/j.tifs.2023.104163>
- Tian, W., Wang, H., Zhu, Y., Wang, Q., Song, M., Cao, Y., & Xiao, J. (2022). Intervention effects of delivery vehicles on the therapeutic efficacy of 6-gingerol on colitis. *Journal of Controlled Release*, 349, 51–66. <https://doi.org/10.1016/j.jconrel.2022.06.058>
- Tie, S., Su, W., Chen, Y., Wu, S., Wu, H., Song, Y., ... Tan, M. (2022). Dual targeting procyanidin nanoparticles with glutathione response for colitis treatment. *Chemical Engineering Journal*, 441, Article 136095. <https://doi.org/10.1016/j.cej.2022.136095>
- Tsuda, T. (2018). Curcumin as a functional food-derived factor: Degradation products, metabolites, bioactivity, and future perspectives. *Food & Function*, 9(2), 705–714. <https://doi.org/10.1039/c7fo01242j>
- Vafaei, S. Y., Esmaeili, M., Amini, M., Atyabi, F., Ostad, S. N., & Dinarvand, R. (2016). Self assembled hyaluronic acid nanoparticles as a potential carrier for targeting the inflamed intestinal mucosa. *Carbohydrate Polymers*, 144, 371–381. <https://doi.org/10.1016/j.carbpol.2016.01.026>
- Wang, C., Tian, W., Song, Z., Wang, Q., Cao, Y., & Xiao, J. (2024). Effects of solid lipid ratio in curcumin loaded emulsions on its gastrointestinal fate: Colloidal stability and mucus absorption efficiency. *Food Research International*, 175, Article 113631. <https://doi.org/10.1016/j.foodres.2023.113631>
- Wang, H., Tian, W., Li, Y., Yuan, Y., Lv, M., Cao, Y., & Xiao, J. (2022). Intervention effects of multilayer core-shell particles on colitis amelioration mechanisms of capsaicin. *Journal of Controlled Release*, 351, 324–340. <https://doi.org/10.1016/j.jconrel.2022.09.041>
- Wu, S., Liu, S., Li, Y., & Feng, J. (2024). Recent research advances in delivery systems based on the assembly of egg white proteins: Structure design and applications in the food industry. *Food Hydrocolloids*, 153, Article 110021. <https://doi.org/10.1016/j.foodhyd.2024.110021>
- Xiao, B., Chen, Q., Zhang, Z., Wang, L., Kang, Y., Denning, T., & Merlin, D. (2018). TNF α gene silencing mediated by orally targeted nanoparticles combined with interleukin-22 for synergistic combination therapy of ulcerative colitis. *Journal of Controlled Release*, 287, 235–246. <https://doi.org/10.1016/j.jconrel.2018.08.021>
- Xing, L., Liu, X., Wu, L., Wu, J., Deng, Y., Li, Q., ... Huang, Y. (2024). Orally hierarchical targeting delivery systems relieve colitis by protecting host mitochondria and modulating gut microbiota. *Nano Today*, 55, Article 102155. <https://doi.org/10.1016/j.nantod.2024.102155>
- Xiong, W., Xiong, S. H., Chen, Q. L., Linghu, K. G., Zhao, G. D., Chu, J. M. T., ... Yu, H. (2021). Brij-functionalized chitosan nanocarrier system enhances the intestinal permeability of P-glycoprotein substrate-like drugs. *Carbohydrate Polymers*, 266, Article 118112. <https://doi.org/10.1016/j.carbpol.2021.118112>
- Xu, J., Chu, T., Yu, T., Li, N., Wang, C., Li, C., ... Nie, G. (2022). Design of Diselenide-Bridged Hyaluronic Acid Nano-antioxidant for efficient ROS scavenging to relieve colitis. *ACS Nano*, 16(8), 13037–13048. <https://doi.org/10.1021/acsnano.2c05558>
- Yuan, Y., Liu, Y., He, Y., Zhang, B. K., Zhao, L., Tian, S. M., ... Li, Y. (2022). Intestinal-targeted nanotubes-in-microgels composite carriers for capsaicin delivery and their effect for alleviation of Salmonella induced enteritis. *Biomaterials*, 287, Article 121613. <https://doi.org/10.1016/j.biomaterials.2022.121613>
- Zhu, L., Yu, T., Wang, W., Xu, T., Geng, W., Li, N., & Zan, X. (2024). Responsively degradable nanoarmor-assisted super resistance and stable colonization of probiotics for enhanced inflammation-targeted delivery. *Advanced Materials*, 36(18), 2308728. <https://doi.org/10.1002/adma.202308728>